A MEASUREMENT OF THE INCLUSIVE BRANCHING RATIO OF CHARGED AND NEUTRAL D MESON DECAYS CONTAINING A NEUTRINO

A Dissertation

Presented to the Faculty of the Graduate School

of Cornell University

in Partial Fulfillment of the Requirements for the Degree of

Doctor of Philosophy

by

Michael Lawrence Weinberger

May 2006

A MEASUREMENT OF THE INCLUSIVE BRANCHING RATIO OF CHARGED AND NEUTRAL D MESON DECAYS CONTAINING A NEUTRINO

Michael Lawrence Weinberger, Ph.D.

Cornell University 2006

This thesis reports the measurement of branching ratios for the inclusive decay of a D meson to a neutrino, measured at the CLEO-c detector. It is fully inclusive as to lepton flavor and into which semileptonic mode the D decays. This analysis is the first direct measurement of the inclusive neutrino branching ratio. It utilizes 187 pb^{-1} of data taken at the $\psi(3770)$ resonance. The measured values are $BR(D^{\pm} \to X\nu) = 29.43\% \pm 0.83 \pm 1.75$, and $BR(D^0 \to X\nu) = 13.52\% \pm 0.28 \pm 0.68$.

BIOGRAPHICAL SKETCH

Michael Lawrence Weinberger was born on December 15, 1975, to Irv and Joan Weinberger. He has one older sister by three years, Andrea, and was the last child, as they were all his parents could handle. He was born in Upper St. Clair township, a suburb of Pittsburgh, Pennsylvania. He would move at 3 years, and at 11 years - each time a half mile west - and still hopes to make it to California in 10,000 years.

He began to play the trombone in the 5th grade, which was a small problem, as he couldn't reach the end of the slide until the 7th grade. He continued to play until college. Mike enjoyed well played music, and playing music, which were usually two different things, but he persevered on.

He started Upper St. Clair High School in 1990, and overlapped with his sister for one year, which started a friendly rivalry which continues to this day.[1] He also started to participate on the high school rifle team, in part to offset the uncoolness of being in the band and his recently discovered love of science.

Michael did very well in high school, except for Spanish, and took as many science classes as the school offered. The poster of the standard model in his physics class intrigued him, and this wondering would serve him well in the sciences. He also found time to visit his sister who was now in college at the University of Michigan, who would take him to basketball games, the Big House to join 107,000 watching football, and let him have his first taste of beer.

After graduating in 1994, it was therefore not surprising that Michael followed her to study at the University of Michigan. He asked and was placed in the honors housing, as this was the closest to main campus, and still gives silent thanks to the housing office for ignoring the request of Tamatha Meek, and putting her in

[1] He is still bitter that she beat his GPA by .001 points

honors housing also. Michael meet Tammie before classes started, and they were going out right after Thanksgiving break.

Michael, although he knew that he wanted to go into science, had not decided whether to pursue physics or chemistry. Freshman year he took a semester of Honors Introduction to Mechanics, and took Organic Chemistry the next semester. He soon discovered that he much preferred the physics method of taking the simple equation to apply to any manner of situations, and trying to simplify thing to their basic components and behaviors. Or he might have just not liked memorizing 200 reactions.

At Michigan, Michael worked for Greg Tarle, helping with the HEAT astrophysics balloon experiment, and also producing aerogels. This was his first experience working on a particle physics experiment, and taught him a lot about how a particle detector worked.

Michael was awarded the Dale and Norman Leff Dean's Merit Scholarship for his junior and senior years, but was not able to convince his parents that he should get a 15% cut of the value of the tuition that he had saved them. The scholarship was awarded to a junior physics major, from out of state, who was planning on continuing on in physics. As proud as his parents and Tammie were of him, he was still convinced that he was the only student who fit the criteria.

After graduating in 1998, and enjoying a new year's spent in Pasadena watching the number-one ranked Wolverines clinch a national championship at the Rose Bowl, Michael and Tammie, who was applying to law schools, tried to end up at the same school. They failed. They did end up in the same city, Philadelphia. Michael started grad school at the University of Pennsylvania, and Tammie began a job.

After a year Tammie decided to attend law school at Cornell University. The physics department was nice enough to allow Michael to transfer, and stay with

her.

After taking classes, he began to work on the CLEO experiment, keeping the gas system going, and working on the new silicon detector calibration. The silicon group morphed into the Rare B analysis group. Michael was lucky enough to be given three modes to analyze, and learned a great deal about how to perform an analysis, which would serve him well for his thesis work.

Michael and Tammie were married on November 23, 2002, finally making their cat, dog, and two rabbits legitimate. Unfortunately, Michael had forgotten to check the calendar, and was, therefore, getting ready to get married while watching the end of the Michigan vs. Ohio State game.

Michael plans to continue on in physics, and to do what always annoyed his parents while he was growing up - ask "why."

This thesis is dedicated to:
Raphael Kapfer who never got a chance to finish his work,
and

Tammie Meek without whom I never would have been able to finish mine.

ACKNOWLEDGEMENTS

First, I would like to thank my family.

Mom and Dad, for all of their support and encouragement through all of my schooling and work for this thesis. And for making sure that I had the opportunity to do what I wanted to do.

Andrea, for leading the way, and showing that it could be done.

Kathy, Bob, Carrie, Ang and Tim, for including me so readily into your family.

I would also like to thank all of my physics teachers in high school, college and grad school for teaching me what I needed to know, and imparting a love of science.

Everyone on CLEO, for providing a great place to learn how to be a physicist. People were always willing to help out with whatever was needed.

Jim Alexander for helping and guiding me through this process. I have learned so much from him about how to be a physicist.

My son Matthew, for making sure that I knew that as important as the thesis was, there was something more important.

And lastly, but definitely most importantly, my wife Tammie, whose support, encouragement, and editing was the only reason I got into, and am finishing grad school. I really couldn't have done it without her. I love you. Really.

TABLE OF CONTENTS

LIST OF TABLES

LIST OF FIGURES

Chapter 1

Introduction

1.1 The Charm Quark

Before its experimental discovery in 1974, there were many predictions that a fourth quark must exist which would be related to the up quark in the same way that the strange quark is related to the down quark. When the charged current was expanded to include the decay of strange particles, it was first written as:

$$J_{\mu}^{(+)} = cos\theta_c \bar{d}_L \gamma_\mu u_L + sin\theta_c \bar{s}_L \gamma_\mu u_L \tag{1.1}$$

However, this extension caused problems as it produces a strangeness changing neutral current, which would cause the predictions for ΔM_K and $K_L \rightarrow \mu^+\mu^-$ to be too high by a number of orders of magnitude. A suppression of the strangeness changing neutral current is accomplished by adding in a fourth quark to balance out the four leptons which were known at the time:

$$J_{\mu}^{(+)} = \bar{d}_{C,L} \gamma_\mu u_L + \bar{s}_{C,L} \gamma_\mu u_L \tag{1.2}$$

with: $d_C = cos\theta_C d + sin\theta_C s$ and $s_C = -sin\theta_C d + cos\theta_C s$

There were also additional theoretical predictions about how the existence of a charm quark would affect other decays. The first of these predictions[1] calculated the effects in the Kaon system's neutral oscillations and various decays.

At first the experimental signatures for the charm were not observed. In the process $e^+e^- \rightarrow hadrons$ the ratio $R = \sigma(e^+e^- \rightarrow hadron)/\sigma(e^+e^- \rightarrow \mu^+\mu^-)$ is

a constant ratio with its value being the sum of the quark charges squared. If only the up, down and strange quarks existed, this ratio would be 2, when the three colors are added in. As measured by Mark I[2], the value was near 2. Later measurements confirmed that R did increase as the J/ψ production threshold was crossed.

In 1974, the J/ψ was simultaneously discovered and announced by two groups[3][4], one at SLAC, and one at Brookhaven. The discovery of the ψ' followed shortly thereafter. The c quark was the first quark to be predicted before its discovery.

The charm quark is the only up type quark whose decays can be studied as a window to the weak force. The top quark is so heavy that it decays before it has time to hadronize. Further, the up quark is only contained in two weakly decaying particles: the neutron and the pion. In the neutron the d quark decays, and in the pion the quarks annihilate. This leaves only the charm as a means to study weak decays. Further, the charm is heavy enough that it can be treated theoretically by expanding in powers of $1/m_c$.

Chapter 2

Theory

2.1 Weak Decays

Figure 2.1 shows the tree level diagram for a basic semileptonic decay of a D meson. The c quark emits a W^+, and becomes an s quark which in turn combines with the original $\bar{u}$ from the D, to form a kaon. The W then decays into a positron and a neutrino.

The interaction term for a W coupling to a quark pair, which is called a weak charged current, is expressed in the Lagrangian by:

$$\mathcal{L}_{int} = \frac{g}{\sqrt{2}}(\mathcal{J}^{\mu}W_{\mu}^{+} + \mathcal{J}^{\mu\dagger}W_{\mu}^{-}) \tag{2.1}$$

with the operator:

$$\mathcal{J}^{\mu} = \sum_{i,j} V_{i,j} J_{i,j}^{\mu} = \sum_{i,j} \mu_i \gamma^{\mu} \frac{1}{2}(1-\gamma_5) V_{i,j} d_k \tag{2.2}$$

The indices i and j run over the three quark generations. The u_i operators annihilate or create the u, c and t quarks, while the d_i annihilate or create d, s, and b quarks. The processes are proportional to the $V_{i,j}$ term, which are matrix elements of the Cabibbo-Kobayashi-Maskawa (CKM) matrix that relate the strengths of the transitions between different states.

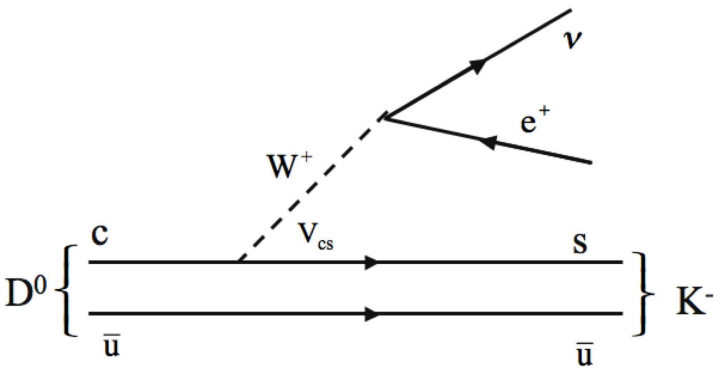

Figure 2.1: Feynman diagram for the semileptonic decay $D^0 \to e^+\nu K^-$

The CKM matrix can be expressed as a rotation between the mass and weak eigenstates. The relation is given by:

$$\begin{pmatrix} d' \\ s' \\ b' \end{pmatrix} = \begin{pmatrix} V_{ud} & V_{us} & V_{ub} \\ V_{cd} & V_{cs} & V_{cb} \\ V_{td} & V_{ts} & V_{tb} \end{pmatrix} \begin{pmatrix} d \\ s \\ b \end{pmatrix}$$

Where the V coupling constants gives the strength of mixing between two quarks. The matrix can be parameterized with three angles, $\theta_{12}, \theta_{23}, \theta_{13}$ and a complex phase, δ_{13}. Using the notation $c_{12} = cos\theta_{12}$ and setting $c_{13} = 1$, given that $V_{ub} = 0.003$, the matrix can be expressed as:

$$\mathrm{V} = \begin{pmatrix} c_{12} & 2_{12} & s_{13}e^{-i\delta_{13}} \\ -s_{12}c_{23} & c_{12}c_{23} & s_{23}c_{13} \\ s_{12}2_{13} - c_{12}c_{23}e^{i\delta_{13}} & -c_{12}s_{23} & c_{23}c_{13} \end{pmatrix}$$

This matrix can be parameterized with the Wolfenstein parameterization which expands in the small parameter $\lambda = sin\theta_c \simeq 0.22$:

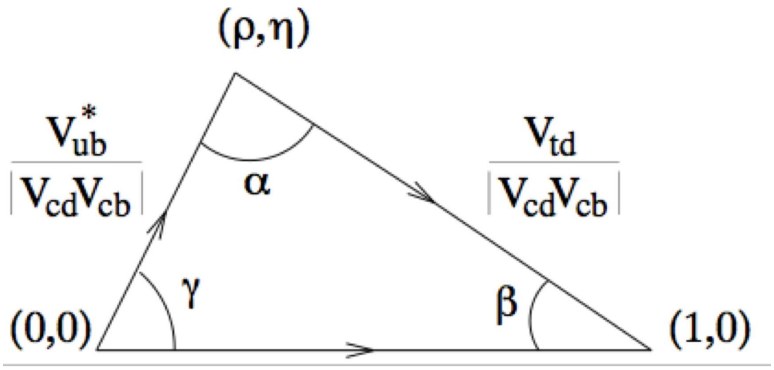

Figure 2.2: Unitary Triangle, with lengths of side in terms of the coupling constants

$$\begin{pmatrix} 1-\frac{1}{2}\lambda^2 & \lambda & A\lambda^3(\rho - i\eta(1-\frac{1}{2}\lambda^2)) \\ -\lambda & 1-\frac{1}{2}\lambda^2 - i\eta A^2\lambda^4 & A\lambda^2(1+i\eta\lambda^2) \\ A\lambda^2(1-\rho-i\eta) & -A\lambda^2 & 1 \end{pmatrix}$$

Using the fact that this matrix is unitary, it is possible to make a number of relations. The most interesting one is : $V_{ud}V_{ub}^* + V_{cd}V_{cb}^* + V_{td}V_{tb}^*$, which is obtained from the first and third columns, which can be parameterized as $A\lambda^3(\rho + i\eta) - A\lambda^3 + A\lambda^3(1-\rho-i\eta)$. This triangle, shown in Figure 2.2, is useful because the side are roughly equal in length, and the angles are not close to either zero or 180 degrees. All of the CP violation from the matrix has now been wrapped up in the imaginary phase η, therefore, if η is equal to zero, there will be no CP violation from this source. The dependance of the amount of CP violation can be seen by the fact that the area of the triangle is $A^2\lambda^6\eta$, therefore, if the area of the triangle is non-zero then there will be CP violation. It is possible to express the length of the sides of the triangle in terms of the coupling constants. The side that connects to the origin has a length of $\frac{V_{ub}^*}{V_{cd}V_{cb}^*}$, and the length of the other side is $\frac{V_{td}}{V_{cd}V_{cb}^*}$.

A large portion of modern weak physics has been focused towards precision

measurements of the sides and angles of the Unitary Triangle. As the measurements of the triangle improve, it will be possible to test the observed measurements versus theoretical predictions to determine possible sources of new physics.

One of the largest limitations on obtaining precision measurements has been the theoretical errors. These errors were between 10% and 20% as calculated by Lattice QCD[5]. Lattice has made incredible strides in recent years in being able to make predictions.[6] These new predictions need to be tested and verified, in part by CLEO-c

CLEO-c will make contributions to this process in many ways. One such way is checks on the calculations of D and D_S, as a verification of the Lattice methods. Once the theoretical predictions that can be currently measured have been checked with experiments, future predictions can be made.

The most direct way in which CLEO-c will have an impact is in the error on the measurements of V_{cd} and V_{cs}. The errors are currently 7% and 16% for V_{cd} and V_{cs}, respectively. With new measurements from CLEO-c, $D \to \pi l \nu$ for V_{cd}, and $D \to K l \nu$ for V_{cs}, these errors will be reduced to a few percent. As each of the constraints on the sides or angles has its error reduced, the area of overlap of the constraints for the vertex will get smaller. As this vertex is constrained, it will either agree with the predictions, or point towards a possible source of new physics.

There are two main reasons that the CLEO-c program will be able to make these incredibly precise measurements. The knowledge of the accelerator gained over multiple decades of running, allows a high luminosity to be achieved. These excellent running conditions give a very large data set which was 30 times the previous $\psi(3770)$ sample from MARK III. This large sample allows rarer decays

to be measured. With such a large sample, tighter cuts can be used to get a purer sample, while still retaining good statistics.

The second reason involves the detector and cleanliness of the sample. Running on the $\Psi(3770)$, which will hadronize entirely to the $D\overline{D}$, means that there will be no extra particles in the event. There will be a far smaller multiplicity of tracks and showers in the events than with the B system. This makes the full reconstruction of the event practical.

With its long history, the CLEO detector is very well understood. The backgrounds from the detector, such as noise from the electronics, or hot or dead channels, have been substantially eliminated from the data. With this knowledge the already clean events are not compromised, and can be fully reconstructed without interference from the extraneous noise and complications from the detector.

2.1.1 Calculation of Spectrum

Although it is not being measured in this analysis; it is informative to examine the spectrum calculation. Examination of the spectrum calculation illustrates how the different decay modes contribute to the overall spectrum.

As stated in the first section of this chapter the quarks couple to the W via the weak current:

$$J^{\mu} = \frac{g_2}{2\sqrt{2}} \bar{\mu}_i \gamma^{\mu} (1 - \gamma_5) V_{i,j} d_j = \frac{g_2}{2\sqrt{2}} V_{i,j} j^{\mu}_{ij} \tag{2.3}$$

The decay rate can then be decomposed into two parts, separated by what quark the c decays to:

$$d\Gamma(\bar{D} \to X e \bar{\nu}) = |V_{dc}| d\Gamma(\bar{D} \to X_d e \bar{\nu})$$

$$+|V_{sc}| d\Gamma(\bar{D} \to X_s e \bar{\nu}) \tag{2.4}$$

As this measurement is inclusive as to the decay products, both of these terms would be included in a calculation. To calculate the decay rate, the transition matrix must be treated first. For semileptonic decay the element is:

$$T = \frac{G_F}{\sqrt{2}} V_{qc} \bar{u_e} (1 - \gamma_5) v_{\nu_e} \langle X_q(p_X s_X)) | j^{\mu}_{qc} | \bar{D}(p_D) \rangle \tag{2.5}$$

One model for treating this calculation is the IGSW[7], which includes hadronic effects, and is more accurate than a free quark model especially at the endpoints. Using the form of the hadronic tensor,

$$h_{\mu\nu} \equiv \sum_{s_x} \langle \bar{D}(p_D) | j^{\dagger}_{\nu} | X(p_X s_X) \rangle \langle X(p_X s_X)) | j_{\mu} | \bar{D}(p_D) \rangle \tag{2.6}$$

Expanding the hadronic tensor gives:

$$h_{\mu\nu} = -\alpha g_{\mu\nu} + \beta_{++}(p_D + p_X)_{\mu}(p_D + p_X)_{\nu} + \beta_{+-}(p_D + p_X)_{\mu}(p_D - p_X)_{\nu}$$

$$+\beta_{-+}(p_D - p_X)_{\mu}(p_D + p_X)_{\nu} + \beta_{--}(p_D - p_X)_{\mu}(p_D - p_X)_{\nu} +$$

$$i\gamma \epsilon_{\mu\nu\rho\sigma}(p_D + p_X)^{\rho}(p_D - p_X)^{\sigma} \tag{2.7}$$

This can be simplified if the mass of the electron is neglected, which eliminates terms with a $(p_D - p_X)$. Using the definitions $x \equiv E_e/m_D$ and $y \equiv (p_D - p_X)^2/m_D^2$:

$$\frac{d^2\Gamma}{dxdy} = |V_{qc}|^2 \frac{G_F^2 m_c^5}{32\pi^3} (\frac{\alpha}{m_c^2} y + 2\beta_{++}(2x(1 - \frac{m_X^2}{m_c^2} + y)$$

$$-4x^2 - y) - \gamma y(1 - \frac{m_X^2}{m_c^2} - 4x - y)) \tag{2.8}$$

The only variables that remain to be calculated are, α, β_{++}, and γ. These can be calculated for each decay mode and then combined to build the inclusive

spectrum. It can easily been seen through the factors $\frac{m_X^2}{m_c^2}$ that the spectrum will depend on which daughter meson the D decays into.

One underlying assumption for making the calculation in this manner is that there is a one to one correspondence between the form factors, f_i obtained from calculating the matrix element $\langle X(p_X s_X))|j^\mu(0)|\bar{D}(p_D)\rangle$, for the physical particles $\bar{D}$ and X, and those from the quark model, $\tilde{f}_i$. The form factor is calculated in the quark method, and then is used to get the values of α, β_{++}, and γ for this method.

The expansion for the physical state is $\langle D|j^\mu(0)|A\rangle = \sum_i f_i(t-t_m)X_i^\mu$, with $t = (p_D - p_A)$, and the maximum transfer $t = (m_D - m_A)$.

We can now look at how the spectrum will differ for two different daughter particles, such as K and K^*. Figure 2.3 shows the electron spectrum for D decays. Figure 2.3 shows separately the spectrum for X being a Kaon in dots, Kaon plus K* in close dots, the total inclusive spectrum as the dark solid line, and the free quark calculation as the light line. The difference in spectrum between the For these calculations the following definition will be used:

$$F_n = \left(\frac{\tilde{m}_X}{\tilde{m}_D}\right)^{1/2} \left(\frac{\beta_D \beta_X}{\beta_{DX}^2}\right)^{n/2} \times exp\left(-\left(\frac{m_D^2}{4\tilde{m}_D\tilde{m}_X}\right)\frac{t_m - t}{\kappa^2\beta_{DX}^2}\right) \tag{2.9}$$

with $\beta_{DX}^2 = 1/2(\beta_D^2 + \beta_X^2)$.

The K is a $1S$ state, while the K^* is a $2S$. For both the axial part will drop out leaving only the vector component, $\langle X(p_X)|V_\mu|\bar{D}(p_D) = f_+(p_D+p_X)+f_-(p_D-p_X)$. From this, $\alpha = \gamma = 0$, and $\beta_{++} = f_+^2$ for a Kaon, and $\beta_{++} = f_+'^2$:

$$f_+ = F_3\left(1 + \frac{m_c}{2\mu_-} - \frac{m_b m_q}{4\mu_+\mu_-}\frac{m_d}{\tilde{m}_X}\frac{\beta_D^2}{\beta_{DX}^2}\right) \tag{2.10}$$

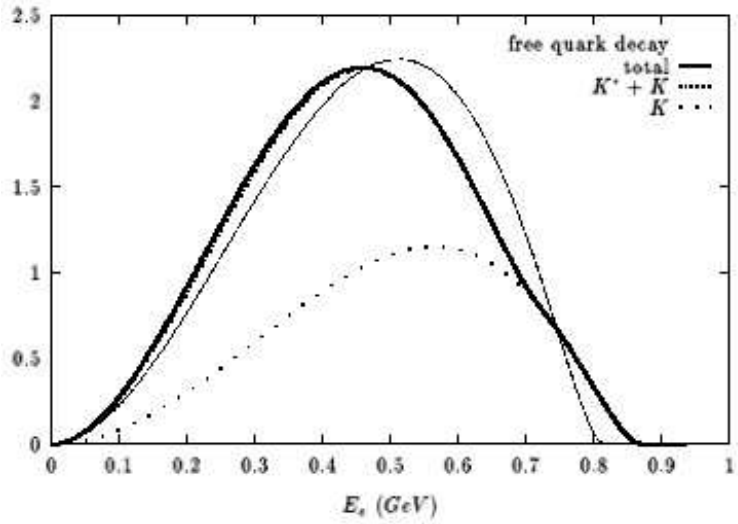

Figure 2.3: The electron spectrum for D decaying to K - dots, K plus $k*$ - close dots, Total Inclusive - heavy solid line, & Free Quark Decay - thin solid line

$$f'_+ = F_3 \left(\frac{3}{8}\right)^{1/2} \frac{m_b}{\mu_+} \frac{\beta_D^2 - \beta_X^2}{\beta_D^2 + \beta_X^2} + \frac{m_q m_d}{3\mu - \tilde{m}_X} \frac{\beta_D^2}{\beta_{DX}^2} \left(\frac{7\beta_X^2 - 3\beta_D^2}{4\beta_{DX}^2}\right)$$
$$+ \frac{1}{6} \frac{m_d^2}{\tilde{m}_X \tilde{m}_D} \frac{\beta_X^2}{\beta_{DX}^2} \frac{t_m - t}{\kappa^2 \beta_{DX}^2} \times \left(1 - \frac{m_q m_d}{2\mu - \tilde{m}_X} \frac{\beta_D^2}{\beta_{DX}^2}\right) \tag{2.11}$$

We can now look at how the spectrum will differ for two different daughter particles, such as K and K^*. Figure 2.3 shows the electron spectrum for D decays. It shows seperatly the spectrum for X being a Kaon in dots, Kaon plus K* in close dots, the total inclusive spectrum as the dark solid line, and he free quark calculation as the light line. The difference in spectrum between the K and K^* can be seen. This can also be explained in terms of the dynamics of the decay, which will be discussed in the next section.

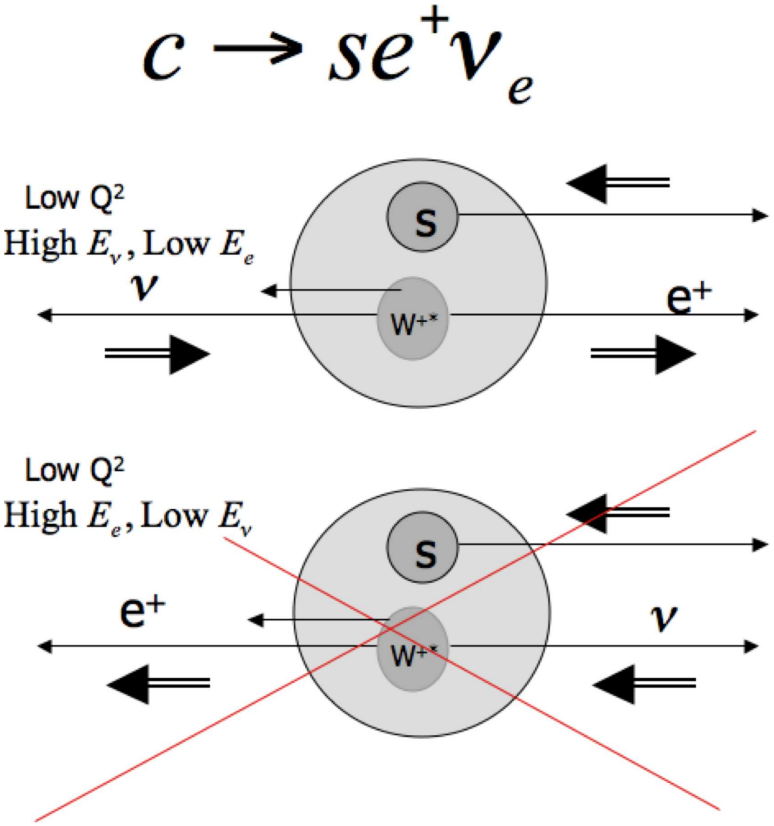

Figure 2.4: Skematic of Charm decay - Top: favored & Bottom: suppressed, due to helicity constraints

2.1.2 Dynamics

To discuss the dynamics of semileptonic decays, one important variable is Q^2, which is the mass squared of the W:

$$Q^2 = m_W^2 = (p_l + p_{\bar{\nu}}) = (P - p_x)^2 = M^2 + m_x^2 - 2ME_x \tag{2.12}$$

with P being the 4-momentum of the initial meson, and X being the resulting non-leptonic component of the decay.

At the Q^2_{max}, most of the available energy is taken up by the mass of the W, leaving the daughter quark mostly at rest. This leads to a large overlap between the daughter and spectator quark, which makes the production of a final state meson more favorable.

At Q^2_{max}, the W is nearly at rest. Being a two body decay, in the rest frame of the W, the charged and neutral leptons will come out back to back. Since the W is nearly at rest in this configuration neither daughter will receive a large boost when transformed into the lab frame. As the Q^2 value is reduced, the W begins to receive a boost in the lab frame. Whichever daughter is traveling in that direction will receive a boost in its energy. Analyzing the helicities of the particles in the interaction will show that the neutrino will have a harder spectrum due to this effect.

At low Q^2, there is a large amount of energy available to give motion to the W and spectator quark. In the rest frame of the W, as in Figure 2.4 which shows the decay $c \to se^+\nu_e$, the positron and neutrino emerge back to back. In the lab frame the s quark will receive a boost in the opposite direction of the W. The s quark and the neutrino, being particles, will be left-handed, while the anti-particle positron will be right-handed. The lower configuration in the plot is highly suppressed as

it is impossible to combine the spins into that of the original c quark.

The top figure in Figure 2.4 shows the favored configuration, where the neutrino is emitted in the direction opposite the s quark. When boosted back to the lab frame, the neutrino will receive a boost from being emitted in the direction of travel of the W. When the c is replaced by an anti-c, the now anti-neutrino will still be emitted in the direction of travel of the W, as all of the spins have been reversed.

This effect is modified by the character of the daughter meson. In a decay to a pseudoscalar, such as $D \to Kl^+\nu$, the helicity information is lost. Given that the daughter has a helicity of zero, and the spin of the initial meson is also zero, the W will necessarily have a helicity of zero.

This is contrary to the case where the daughter meson is spin one, such as a K^*. The helicities are kept and, since the daughter meson has a higher probability of being -1, this will affect the angular distribution of the leptons. It will cause the neutrino to be emmited preferentially in the direction of the travel of the W.

2.2 Heavy Quark Expansions of the Charm System

This section will describe different theoretical methods of calculating the physics of weak decays; specifically, the inclusive semileptonic decays of the D.

There are various theoretical methods available to treat the charm system, because the charm quark is considered a "heavy" quark relative to other "light" quarks with which it combines to form a particle. In a general treatment, this is referred to as using an Effective Field Theory. The problem can be split up

depending on what the energy scale is in relation to the masses of the fields. Taking two fields, Φ_i and ϕ_j with masses M_{Φ_i} and m_{ϕ_j}, the Lagrangian can be examined for different regimes. For $\mu \gg M_{\Phi_i}$, the theory is assumed to be asymptotically free so that the interactions between the field can be treated perturbatively. As the energy scale lowers to $M_{\Phi_i} > \mu > m_{\phi_j}$ only the light fields will contribute operators to the Lagrangian. The heavy fields will contribute through quantum corrections in the form of coefficients, c_i

$$\mathcal{L}(\mu \gg M_{\Phi_i}) = \sum_i c_i \mathcal{O}_i(\Phi, \phi) \Rightarrow \mathcal{L}(M_{\Phi_i} > \mu > m_{\phi_j}) \simeq \sum_i \bar{c}_i(\Phi)\bar{\mathcal{O}}(\phi)) \tag{2.13}$$

Heavy Quark Expansions

These methods use the mass of heavy quark as an expansion parameter of the QCD Lagrangian. At a scale greatly above the mass of the heavy quark, the Lagrangian is split into two parts, one that contains the heavy quark, and one that has the light degrees of freedom.

$$\mathcal{L}_{QCD}(\mu \gg m_Q) = \mathcal{L}_{light}(\mu \gg m_Q) + \mathcal{L}_{heavy}(\mu \gg m_Q) \tag{2.14}$$

$$\mathcal{L}_{light}(\mu \gg m_Q) = -\frac{1}{4} G_{\mu\nu} G_{\mu\nu} + \sum_q \bar{q} i(\not{D} - m_q) q \tag{2.15}$$

$$\mathcal{L}_{heavy}(\mu \gg m_Q) = \sum_Q \bar{Q}\rangle(\not{D} - m_Q) Q \tag{2.16}$$

Operator Product Expansion

The next theoretical method needed is the Operator Product Expansion[8]. This method allows for an expansion in inverse powers of the mass of the heavy quark, while putting the short distance dynamics into coefficients of the expansion. A scale, μ, is introduced, which splits the degrees of freedom into two regimes.

Above this scale the heavy quark degrees of freedom are integrated out and their contributions are contained in the Wilson Coefficients, c_i, while the degrees of freedom below the scale μ still appear as dynamical operators. As per [9] the width for a hadron containing a heavy quark can be written as:

$$\Gamma(H_Q \to f) = \frac{G_F^2 m_Q^5(\mu)}{192\pi^3}|V_{CKM}|^2[c_3(m_f;\mu)\langle H_Q|\bar{Q}Q|H_Q\rangle|_\mu +$$
$$c_5(m_f;\mu)\frac{\mu_G^2(H_{Q,\mu})}{m_Q^2} + \sum_i c_{6,i}(m_f;\mu)\frac{\langle H_Q|(\bar{Q}\Gamma_i q)(\bar{q}\Gamma_i Q)|H_Q\rangle|_\mu}{m_Q^3} + \mathcal{O}(1/m_Q^4)] \quad (2.17)$$

with $mu_G^2(H_{Q,\mu}) \equiv \langle H_Q|\bar{Q}\frac{i}{2}\sigma \cdot GQ|H_Q\rangle$

2.2.1 Lifetimes and f_D

The decay of the c quark, to leading order governs the decay of a charm hadron, with the light quark acting as a "spectator" to the decay. The lifetime is expressed by:

$$\Gamma_{spect} \propto G_F^2 m_c^5 \quad (2.18)$$

This would indicate that the lifetimes of the D^0 and the D^+ should be equal, with small corrections. However, the lifetime ratio is measured to be about 2.5. There are two mechanisms which could affect this, Pauli Interference, and Weak Annihilation (WA). Pauli Interference results from there being two identical quarks in the final state, which then causes an interference term. Weak annihilation will change the ratio since W exchange is Cabibbo favored for D^0 and suppressed for D^+ [10].

Using the machinery described thus far, a prediction can be made as to the ratio of the charged and neutral semileptonic decays. This derivation will follow Bianco.[11] Using HQE, the width for decay of a heavy meson to a final state is

given as:

$$\Gamma(H_Q \to f) = \frac{G_F^2 m_Q^5}{192\pi^3}|KM|^2 \left[A_0 + \frac{A_2}{m_Q^2} + \frac{A_3}{m_Q^3} + \mathcal{O}(1/m_Q^4)\right]. \tag{2.19}$$

When calculating a ratio of lifetimes, the dominant order is $1/m_Q^3$ and not $1/m_Q^2$. As previously explained, there are no contributions of $\mathcal{O}(1/m_Q)$ due to exact cancellations between the initial and final states[12]. These cancelations still act upon $\mathcal{O}(1/m_Q^2)$, giving them a smaller value then they would normally have. These cancelations do not arise once the calculations reach $\mathcal{O}(1/m_Q^3)$ therefore there is no reduction in strength for this term, making it stronger than the suppressed $\mathcal{O}(1/m_Q^2)$.

The decay widths of D^0 and D^+ have the same contribution from the A_0 term, which is from the spectator diagram. The same is true of the A_2 term[13]. The $1/m_Q^3$ however, will introduce a difference in the lifetimes. Pauli Interference will contribute to D^+, while Weak Annihilation will add to D^0. However, due to various suppressions calculated from HQE[14], from helicity and being nonfactorizable, Weak Annihilation will not contribute greatly to this term. As there is no similar suppression the D^+ term, this causes a difference in the lifetimes:

$$\Gamma(D^+) \simeq \Gamma_{spect}(D^0) + \Delta\Gamma(D^+) \tag{2.20}$$

$$\Delta\Gamma(D^+) \simeq \Gamma_0 \cdot 24\pi^2(f_d^2/m_c^2)\kappa^{-4}$$
$$\cdot \left[(c_+^2 - c_-^2)\kappa^{9/2} + \frac{1}{N_C}(c_+^2 - c_-^2) - \frac{1}{9}(\kappa^{9/2} - 1)(c_+^2 - c_-^2)\right] \tag{2.21}$$

With

$$\kappa = [\alpha_s(\mu_{had}^2)/\alpha_S(m_c^2)]^{1/b}, b = 11 - \frac{2}{3}N_f \tag{2.22}$$

The difference in the lifetimes is then expressed fully in terms of PI. Looking at experimentally measured ratios of f_D and f_{DS}, and using the fact that with the WA

suppressed gives $\Gamma(D^0) \simeq \Gamma_{spec}(D) \simeq \Gamma(D^+)$, one reaches the following expression for the ratio of the lifetimes:

$$\frac{\tau(D^+)}{\tau(D^0)} \simeq 1 + (\frac{f_D}{200MeV})^2 \tag{2.23}$$

Using Isospin symmetry we can say that the semileptonic decay widths for D^0 and D^+ should be equal

$$\Gamma(D^0 \to Xl\nu) = \Gamma(D^+ \to Xl\nu) \tag{2.24}$$

and with the Branching Ratio:

$$BR(D \to Xl\nu) = \frac{\Gamma(D \to Xl\nu)}{\Gamma(D \to X)} \tag{2.25}$$

leading to:

$$BR(D^0 \to Xl\nu) * \Gamma(D^0 \to X) = BR(D^+ \to Xl\nu) * \Gamma(D^+ \to X) \tag{2.26}$$

and with $\Gamma = 1/\tau$

$$\frac{BR(D^0 \to Xl\nu)}{\tau_{D^0}} = \frac{BR(D^+ \to Xl\nu)}{\tau_{D^+}} \tag{2.27}$$

resulting in:

$$\frac{BR(D^+ \to Xl\nu)}{BR(D^0 \to Xl\nu)} = \frac{\tau_{D^+}}{\tau_{D^0}}. \tag{2.28}$$

We can then express the ratio of lifetimes relating it to f_D in terms of the Branching Ratio

$$\frac{BR(D^+ \to X\nu)}{BR(D^0 \to X\nu)} \simeq 1 + (\frac{f_D}{200MeV})^2 \tag{2.29}$$

Putting in the value of f_D, found from the recent CLEO-c measurement of $D \to \mu\nu$ [15], $f_D = 222.6 \pm 16.7^{2.8}_{3.4}$, yields a value for the ratio of branching ratios of 2.239 ± 0.856. The ratio of BR found from this analysis is 2.217 ± 0.169. These ratios agree very well, giving confidence in the BR result.

Chapter 3

Detector and Monte Carlo

The incredible strides that have been made in particle physics would not have been possible if there had not been concurrent improvements in the hardware that produce and detect the particle interactions being measured. Accelerators have been improved to collide beams at higher energies to access higher mass initial state particles, while increased luminosity has allowed investigations into decays that are increasingly rare. The colliding particles are accelerated to specific energies which determine the outcomes of their collision. The byproducts of these collisions are recorded by the detector which surrounds the interaction region. When the reactions of each daughter particle in each sub-detector are combined, the identity of each daughter can be found. These daughters can then be combined to determine into what the accelerated particles decayed.

3.1 Accelerator

The accelerator is responsible for producing the particles that decay and are then measured for the various analyses performed. There are many different parts of the accelerator, each of which perform a different, but necessary, function to produce good physics results. CESR accelerates and collides electrons and positrons, which simplifies some of the problems in accelerating particles to the high energies needed for modern particle physics, as will be discussed below. Figure 3.1 shows a picture of the different parts that comprise CESR and the synchrotron.

3.1.1 Accelerating the Particles: The Synchrotron

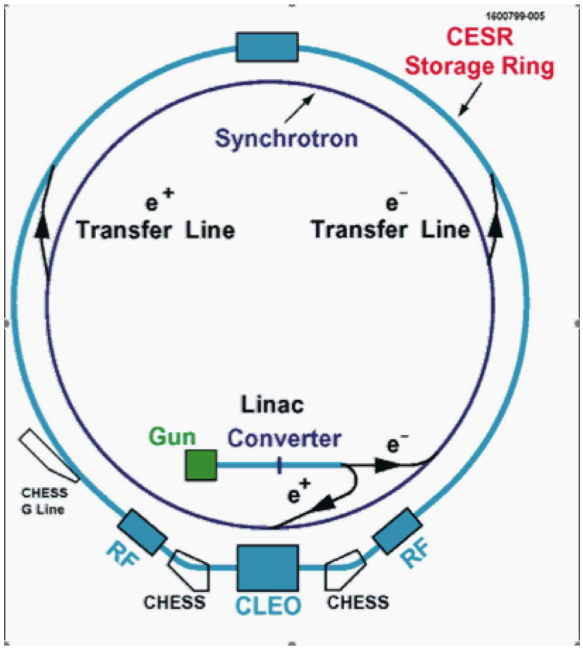

Figure 3.1: Schematic of the Syncrotron and CESR

In the first stage of acceleration, the electrons are produced by an electron gun, which is a cathode filament where the electrons are boiled off by the high temperature caused by the current passing through it. These electrons, which have an energy of 150 KeV, are then passed through their first acceleration in the linac, which is a linear accelerator. The accelerating components of the linac are a series of microwave cavities.

The acceleration is performed by carefully controlling when the particles enter the cavity with respect to the oscillating electric fields. The first condition is that the electric field is pointing the correct direction to accelerate the particles. It may seem obvious that the cavities need to be set up in this manner, but this does mean that half of the time the cavity is on, it is not useful for accelerating particles.

In addition to accelerating the produced electrons, the Linac also bunches the particles as they travel down its length. At first glance it would seem logical for the particles to be accelerated at the maximal strength of the electric field. However, this would cause these bunches to get spread out, which can be seen by looking at three example particles. The middle particle, which will be at the peak of the accelerating wave, will be called "ideal", and will be assumed to act in a manner that is the most desirable. The particle which arrives before the ideal one will receive less of a boost, and will slow down relative to the ideal particle, which is desirable if the particles are being bunched. However the particle that arrives after the ideal one will also receive less of a boost. This means that any particle arriving before or after the ideal one will fall increasingly behind.

Particles can be bunched by only utilizing the accelerating cavities when the electric field is increasing. The ideal will now receive less energy boost, but the gain is in the natural corrections made to slower or faster particles. Since the electric field is increasing, a faster particle will now get less of a boost, and will slow down relative to the ideal particle. Additionally, slower particles will now get more of a boost, speeding them up to catch up with the ideal particle. In this way the particles are bunched and any particle that does not reach the accelerating cavity at the correct time will be corrected back to the ideal. This method of correction made by the different boosts to particles which reach the cavity either early or late is also used in the accelerating cavities in the next two parts of the accelerator.

As the particles get accelerated to higher energies in the circular parts of the machine, this condition will switch so that higher energy particles will arrive after the ideal particle, and lower energy particles will arrive before it. Although this seems counterintuitive, it is a natural consequence of how the particles behave as they are accelerated. As the particles reach higher energies, they approach the

speed of light asymptotically, which leads to a smaller difference in speed between particles as the overall energy scale goes up. The higher energy particles will be bent less in the magnets that keep the particles going in a circle, meaning that they will have a longer path to travel around the machine. As such, the higher energy particles will, because of the longer distance they travel, arrive at the accelerating cavity later. To counteract this, instead of using the cavities when the electric field is increasing, the particles now pass through when the field is decreasing. As such, the higher energy particle, arriving after the ideal particle, will get less of a boost. Therefore, each particle that does not have the ideal energy will be moved toward the ideal energy.

When the electrons leave the linac, in bunches 14ns apart, they have been accelerated to 300 MeV. In the middle of the Linac is an insertable tungsten target which is used to produce the positrons. The 150 MeV electrons smash into the target, and the positrons are funneled out from the other resulting particles produced. The particles, either the electrons or positrons, then move into the next section of the accelerator, the synchrotron. The electrons and positrons are injected into the synchrotron going in opposite directions.

As the particles are injected from the linac into the synchrotron, their path must be bent. The synchrotron is the first major part of the the accelerator which requires bending of the particles. The synchrotron is contained in a ring 768 meters in circumference. Bending the particles is a relatively simple procedure. The ring, in addition to the accelerating sections, is composed of dipole magnets, whose magnetic fields are oriented in the vertical direction. As the electrons pass through the magnetic field, they are bent in the horizontal direction. The positrons, which are traveling in the opposite direction, are bent in the direction opposite to the electrons due to their opposite charge. This allows both the electrons and positrons

to be bent in a direction necessary to keep them in the ring. As the momentum of the particles is increased up to their final energy, the strength of the magnetic field is also increased. The bending of a charged particle is proportional to its momentum and the strength of the magnetic field. In order to keep the accelerating particles traveling in a ring, the magnets must be ramped up to maintain a constant bending radius.

The particles spend only 10 milliseconds in the synchrotron while they are accelerated up to their full energy of 1.886 GeV. This process is repeated at a rate of 60Hz. After the particles are accelerated to their final energy, they are transfered to the Cornell Electron Storage Ring (CESR).

3.1.2 Colliding The Beams: CESR

The main benefit of colliding two beams into each other, instead of smashing a beam into a fixed target, is in the energy accessible to make new particles.

$$\text{Fixed Target:} E_{available} = \sqrt{E m_{target}} \tag{3.1}$$

$$\text{Colliding Beams:} E_{available} = 2E \tag{3.2}$$

For colliding beams, all of the energy is available, giving 2E, with E being the energy of one beam. For a fixed target collision only $\sqrt{E}$ can be used to make new particles. The remaining energy is used in the acceleration of the resulting products which travel in the direction of the initial beam in order to conserve momentum.

In CESR the beams of electrons and positrons are collided with equal energy. This symmetry in the beams means that the center of mass of the collisions is

almost the same as the lab frame of reference. There is a small crossing angle resulting in the center of mass being slightly boosted with respect to the lab frame. This simplifies the reconstruction of the event, as the particles do not need to be boosted significantly to get them to the center of mass frame. The other benefit is that the detector can also be built symmetrically around the interaction point.

In addition to the bending magnets there are two other types of magnets: focusing and correcting. Having separate magnets to bend and focus the beam makes CESR a separate function machine. The focusing magnets are quadrupole magnets, with four alternating poles, two north and two south. The field for this magnet focuses in one direction, and defocuses in the other direction. These quadrupoles are placed in between each bending dipole, and the direction of the focusing is alternated, so that the beam will be focused in the x direction, and then the y. When the properties of the magnets are carefully selected, the overall effect will be the beam being focused in both directions.

Correction magnets make modifications to the beam as it travels around the accelerator. These corrections help with the stability of the beam. The chromaticity of the beam – the focusing's dependence on the momentum of the particle – is corrected by sextupole magnets. These corrective magnets are interspersed between each dipole magnet.

Another example of a magnet used to make a correction to the beam are skew quads which fix linear coupling. The motions of the particles in x and y are not independent but are mixed primaily by two sources: magnets that have a slight rotation to them, or by a solenoid magnet, which acts as a quadrupole rotated by 45 degrees. To fix this problem, quadrupole magnets are placed in the ring with a skew angle that will cancel out the linear coupling from the rest of the ring.

As the electrons are accelerated around the ring they lose energy due to synchrotron radiation. As a particle undergoes any acceleration, either by changes to its speed or its direction, it will produce this radiation according to the equation for its power loss:

$$P = \frac{1}{6\pi\epsilon_0}\frac{e^2a^2}{c^3}\gamma^4. \tag{3.3}$$

With $a = v^2/\rho$ the centripetal acceleration of a particle traveling with speed V in a machine that has a radius of curvature ρ. As the particle speed approaches the speed of light, the equation when the numerical factors are combined, becomes:

$$W = 8.85x10^{-5}E^4/\rho MeVperturn \tag{3.4}$$

This energy loss, if not countered, would cause the beam to be lost. The dipoles for CESR, unlike the synchrotron, have a static field and do not change to account for varying energies of the beam. Therefore as the particles lose energy, they would be bent more and more, until they would collide with the inner wall of the beam pipe and be lost. This would limit the beam lifetime to about 50ms.

To correct for this lost energy, energy is replaced by means of superconducting RF cavities. These operate the same as the accelerating cavities in the synchrotron, but instead of accelerating the beams, they are designed to keep the energy of the beam at a constant value. These RF cavities are superconducting, which has several benefits over the traditional technologies. With superconductivity comes the elimination of electrical resistance leading to power consumption several hundred times less than normal cavities.

More importantly, the physical aperture can be much larger. Normal cavities have a much smaller aperture to reduce power loss, but this extreme narrowing limits the accelerator's possible maximum current. With superconducting cavities,

the aperture can be much larger. For CESR, it was possible to triple the size of the aperture. Additionally, since the superconducting cavities can sustain a larger accelerating gradient, the length of the cavities can be shorter. A shorter accelerating cavity will cause less disruption to the beam.

Though the production of synchrotron radiation energy requires the existence of extra accelerating machinery in the storage ring, it also has beneficial properties that help with the stability of the beams. Since the particles pass through the ring billions of times during a run, any small deviation in the magnets or accelerating cavities would be multiplied with each pass, and therefore so would the error. The radiation emitted by the particles effectively wipes out this memory of the errors.

Additionally, this emitted energy is very useful for reducing the time it takes to inject the particles into the beam pipe. There is a reference trajectory that the "perfect" particle would follow each turn around the accelerator, and the path around which all non-perfect particles oscillate. When a bunch is injected into the storage ring, it needs to dampen down to this "perfect" orbit before the next bunch is injected, otherwise the interactions with the next bunch may make it unstable, resulting in the loss of the newly injected bunch. The damping time therefore determines the minimum time between the injection of bunches, and therefore also determines the overall time to fill the machine. Going from the $\Upsilon(4S)$, where the fill time starting with an empty machine was approximately 5 minutes, to the lower energy at the $\Psi(3770)$, a large problem was the increase in fill time. With the lower energy synchrotron radiation being emitted from the beams, the filling time would increase to over an hour.

To decrease the filling time, and improve the stability of the beams, an additional source of synchrotron radiation is added to the machine. This was accom-

plished by the insertion of wiggler magnets into the storage ring. These magnets are composed of a series of alternating dipole magnets with their fields in the vertical direction. As such, a particle passing through one of these magnets would first be bent to the left, then to the right, and so on, finishing with the same direction of travel as if the magnet were not there. This alternate bending causes synchrotron radiation, which replaces some of the radiation not emitted due to the lower energy running conditions. Twelve such magnets have been placed in the storage ring to produce this extra radiation.

Unlike some other accelerators, CESR has only a single beam pipe which is shared by the electrons and positrons. In order to have the highest possible luminosity, and to use the machine to its highest capacity, the maximum stable number of particles should be in the machine at one time. There is a limit to the amount of particles that can be put into one bunch - this is a function of the fact that all of the particles in the bunch have the same charge and repel each other. Once this limit is reached, the method to permit more particles in the machine is to have multiple bunches. As previously described, the slope and direction of the accelerating field is used to focus the bunch in the energy and time dimensions. Each time the accelerating cavities goes through one cycle, there is a stable point of acceleration at which a bunch can be placed. The theoretical maximum number of bunches is then determined by the frequency of accelerating cavities and the time it takes a bunch to make one revolution. The actual number is smaller than this theoretical maximum due to other considerations, such as beam - beam interactions.

If there were only two bunches in the storage ring at one time, one of particles and one of anti-particles, then they would collide inside the detector, and on the opposite side of the ring. As more bunches are placed into the storage ring, parasitic

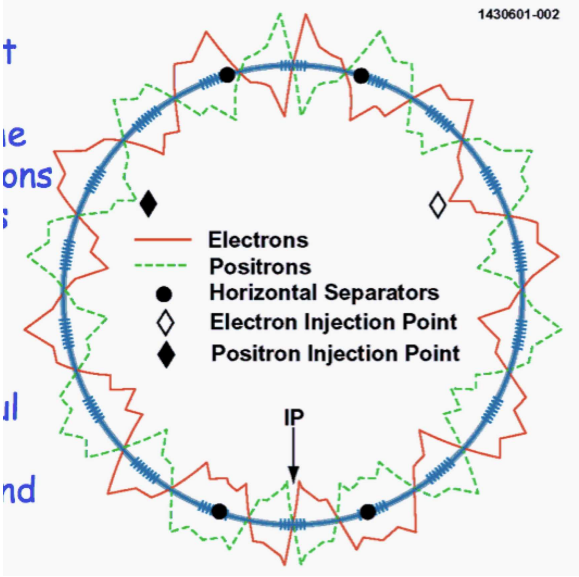

Figure 3.2: A picture of CESR showing the pretzel orbits of the the two beams

crossings increase. Any collisions that occur outside the detector are essentially wasted, as the resulting particles cannot be detected. A scheme was developed at CESR so that the bunches do not interact at these parasitic crossings. The Pretzel Orbit, shown in Figure 3.2, works by having electrostatic separators which perturb the beams from their fixed stable orbit. The bunches then oscillate around this fixed orbit. By carefully tuning the displacements given to the bunches, whenever a bunch of positrons and a bunch of electrons pass each other, not in the detector, they are displaced and no collisions occur. This system of perturbations is set up in a symmetrical manner around the ring, which means, unless corrected for, the bunches would also collide at the point in the ring opposite CLEO. At this point there are vertical electrostatic separators set up so that the bunches pass above and below each other.

This process then allows multiple bunches to be kept in the storage ring at one time, maximizing the use of the machine, and increasing the luminosity. The

machine was run with a maximum of 8 trains of 5 bunches each for the particles and anti-particles, which gives 80 total bunches in the machine at one time.

A great deal of work has to be done to get a clean accelerating and colliding environment which enables good physics to be performed. Through this hard work CESR has provided excellent quality data for CLEO to use.

3.2 The CLEO-c Detector

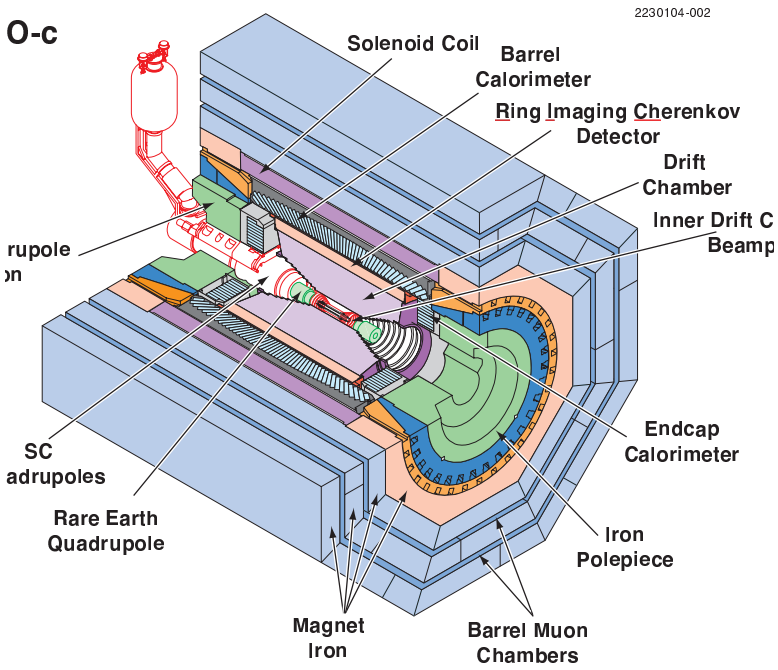

Figure 3.3: The CLEO-c Detector

Once the accelerator brings the electrons and positrons together in a collision, the CLEO-c detector[18][19][20], shown in Figure 3.3, gathers data on the resulting particles as they exit the interaction region. The detector surrounds the interaction point gathering information on each particle as it interacts in the different parts of the detector. Different types of particles leave different signatures in the various subdetectors, and this information is used to determine the particle's type. When the interactions in the subdetectors are examined, the information can be combined to find properties of the particles, such as their energy and momentum.

3.2.1 The ZD and Tracking Chamber

The two innermost subdetectors that the daughter particles pass through are drift chambers, the Z Drift Chamber (ZD) and the Tracking Chamber. These detectors obtain information about charged particles. They give measurements of the charge, momentum, and dE/dx which are used for particle identification. These detectors are built as two symmetric cylinders surrounding the interaction region. This section first describes how a drift chamber works in general, and then describes the specifics of the CLEO-c chambers.

Drift chambers are filled with a gas that the daughter particles ionize as they pass through the detector. The electrons which are produced are then collected and are used to gather information about these particles.

The detection elements of these tracking chambers are sense wires which are held at a voltage of 2 KV, and field wires which are held at ground. These wires run the length of the detector and parallel the beam pipe. These wires define a sense cell. In this cell the electrons produced by the ionization from the particle

which traversed the cell are collected by the sense wire. The wires set up an electric potential difference which guides the produced electrons toward the sense wire.

The drift speed of electrons in the Helium - Propane gas mixture used in the detector is known. Therefore, the time it takes the first ionized electrons to reach the sense wire can be used to determine where the particle passed through the sense cell. The cells in the different layers are staggered by one half cell around the beam pipe, to determine which side of the the drift cell the electrons passed through. This allows a very precise determination of the location of the track in the drift cell. For CLEO-c the resolution on the location of the track in the cell can be measured within an average of 85 μm.

These hits give very accurate information on r and ϕ, the transverse distance from the beam pipe and the azimuthal angle around the beam pipe, respectively, but give no information on the z axis, the distance measured along the beam pipe. It is important to have information about all three coordinates when the tracks are being combined to try to reconstruct the event. In order to measure this z displacement some of the layers of cells must not be perfectly parallel to the beam pipe. These stereo layers have a slight angle with respect to the parallel layers, as if the endcap were twisted like a lid on a jar, which will twist the wires around the beam pipe. Therefore, as a particle goes from a parallel layer to a stereo one, which cell it passes through will depend on its z coordinate. Given this structure, when a particle passes through the drift chamber, the combination of which parallel and stereo layers have hits gives z information about the track.

At the outermost skin of the Drift chamber is a set of cathode pads which are used to contain the field pattern. These are segmented in the z direction, and are read out to give additional z information.

Another way in which drift chambers give information about the particles that traverse them is by looking at the amount of energy the particle leaves as it moves through the detector. The amount of energy that a particle will lose to ionization is dependent on its velocity. This relationship is given by the Bethe-Bloch equation:

$$-\frac{dE}{dx} = kz^2\frac{Z}{A}\frac{1}{\beta^2}\left[\frac{1}{2}ln\frac{2m_ec^2\beta^2\gamma^2T_{max}}{I^2} - \beta^2 - \frac{\delta}{2}\right] \tag{3.5}$$

Therefore, by using the average specific ionization, dE/dx, along with the measurement of the momentum, it is possible to make an identification of the particle, as different particle types will have different dE/dx for the same momentum.

The CLEO-c tracking consists of two chambers, the larger Drift Chamber (DR), and the inner chamber, the ZD. In CLEO III the innermost detector was a 4-layer silicon microstrip detector. This was replaced for the running at lower energy for a number of reasons. The first and most important reason has to do with the amount of material that is contained in the silicon detector. The lower energy particles will scatter off the material in the detector. This will degrade the measurement of the tracks. At the lower end of the momentum spectrum, and especially in the psi(3770) running regime, this scattering will make a momentum measurement impossible. Another reason that the silicon is not needed in CLEO-c is that it was designed to make precise measurements of the vertex of decays in CLEO III. The D mesons do not travel far enough to make vertexing practical for measurements.

The outer main tracking chamber covers from 12 cm to 82 cm in the radial direction. It is composed of 47 layers of cells, with the inner 11 layers being parallel ones. The next 36 layers are stereo layers. They are grouped into superlayers of 4 layers, which alternate their stereo angle. In order to get good z information as the track is projected to the interaction point, the new inner tracking chamber, which covers from 4 to 12 cm radially, has all of its layers containing a stereo angle

of 12 - 15 degrees. It has 6 layers, with 300 cells total. To keep the cell size the same throughout the detector, the number of cells per layer would vary from 34 in the inner layer to 66 in the outer layer.

To get the best luminosity possible, it is preferred that the final focusing magnets be placed as close as possible to the interaction region. In the CLEO II.v tracking chamber, the endplate was flat, meaning that the magnets could be placed no closer than the end of the chamber. In order to move the magnets in closer to the interaction point, the CLEO III chamber was designed with a "Wedding Cake" endplate, as seen in Figure 3.3. This allows the magnet to be inserted into the drift chamber, without losing much solid angle coverage. The solid angle that the drift chamber covers is then 93% of 4π.

3.2.2 The RICH detector

In the upgrade from CLEO II.V to CLEO III, a Cherenkov detector was added to help in particle identification. The RICH, or Ring Imaging CHerenkov detector, is used in conjunction with the dE/dx information from the tracking chamber to give a measure of what kind of particle is responsible for making a particular rack.

Cherenkov detectors work by detecting the Cherenkov radiation produced by a particle as it passes through matter. When a particle is traveling through matter with a speed greater than the speed of light in that medium, Cherenkov light is produced. This light is produced in much the same way as a shockwave from an airplane traveling faster than the speed of sound. The angle of the light produced is a function on the speed of the particle,

$$cos\theta = \frac{1}{n\beta} \tag{3.6}$$

with θ being the angle of the light emitted with respect to the particle's direction of motion, n being the index of refraction in the material, and $\beta = v/c$ where v is the velocity of the particle. Particle identification can be achieved through an examination of the differentiation of the light cone. This differentiation is maximized by a careful selection of the radiator material based upon the energies of the particles.

The main drawback to the RICH detector is its solid angle coverage, which is only 83% of 4π. As such, a number of tracks which pass through the tracking chamber will not hit the RICH because of the angle with which they leave the interaction region. Additionally, due to distance from the interaction region to the RICH, tracks must have a minimum amount of transverse momentum to reach the detector. If the particle lacks this minimum momentum, it will be bent back towards the beam pipe before it reaches the RICH. At the magnetic field of one Tesla, where the CLEO magnet is run for CLEO-c operations, this minimum momentum is 120 MeV/c. A track with momentum less than this will curl in the tracking chamber, and not reach the RICH.

As a particle traverses through the RICH, it passes through different layers of the detector, each with a different purpose. The first layer they encounter is the part of the detector in which the photons are produced. This is comprised of 1.7cm thick crystals of Lithium Fluoride. This is the only part of the detector in which the particles create the Cherenkov light, the rest of the detector is used to detect the Cherenkov photons.

In the four rings of radiators at the center of the detector, the particles will hit with almost normal incidence. The angle that the light that one of these particle would produce, would hit the outer surface and have a great deal of loss due to

total internal reflection. To overcome this problem, the outer surface is not flat, but is in a sawtooth pattern which presents a different angle of the surface for the light to pass through.

The photons next pass through an expansion gap, with a width of 15.7cm. This gap is filled with nitrogen gas, which allows the light cone to expand to a reasonable size for detection. After this region the light cone passes through a CaF_2 window into multi-wire proportional chamber where it is detected by cathode pads. The chamber is filled with a methane-TEA mixture.

The identification efficiency is dependent on the number of photons detected. When three or more photons are available, the identification efficiency for kaons is 92% with a pion fake rate of 8%.

The RICH detector, when combined with the dE/dx from the tracking chambers, is very good at identification of hadrons, which is very important to this analysis. Without the correct reconstruction of all of the particles in the event, this analysis would not be possible to perform.

3.2.3 The Crystal Calorimeter

The next detector that the particles pass through is the electromagnetic crystal calorimeter. This sub-detector is utilized in measurements of the energy of the particle, and in particular neutral particles. The tracking chambers provide information about charged particles, such as electrons, muons, and charged pions or kaons. Particles such as photons, π^0 and K_L^0 will not interact in the drift chamber, so the calorimeter is where the information about the particles can be obtained.

The 7800 crystals that compose the calorimeter are made of thallium doped cesium iodide, where the thallium is used to tune the energy levels so that the probability of interacting, and the detection of the produced photons, is maximized. They have a face of $5 \times 5cm$, and a length of 30cm, which is 16 radiation lengths. The crystals are arranged so that an incident particle will hit the face of the particle head on, and will travel the length of the crystal. However, the crystals are shifted slightly from directly pointing at the IP. This is done so that a particle cannot pass through a crack between two crystals.

The detector is built in three sections: the barrel and two endcaps. The full detector covers a range of $\cos\theta < 0.93$. The center barrel region covers $|cos\theta| < 0.8$. The outer parts are covered by the endcaps, which fit into the ends of the detector to give almost complete coverage of 4π. The endcap crystals are also arranged with a slight cant to avoid having particles pass between crystals.

The calorimeter's main purpose is to detect the energy of electromagnetic particles; specifically, electrons and photons, and secondarily, to get the energy of hadrons as possible. The difference in design comes from how the particular type of particle interacts within the crystals. The electrons and photons interact with the material primarily through bremmstralung radiation, caused by interaction between the particle and the electrons in the atoms, and by the production of a positron-electron pair. These secondary particles can cause a chain of interactions as they propagate through the material. The total light produced is proportional to the energy of the incident parent particles. Energy showers in a material have a characteristic length, which describes how far into the crystals the shower will progress. For cesium iodide, this length, X_0, equals 1.86cm. This extremely short length, compared to the length of the crystals, 30cm, allows the calorimeter to have all of a electro-magnetic particle's energy deposited in the crystals.

This is in contrast to the hadron's interactions in the crystals. Hadrons will lose energy in the crystals due to nuclear interactions, such as inelastic scattering. This interaction will have a much longer characteristic length, $\lambda = 37cm$. To get the same number of interaction lengths as for the electromagnetic interactions, the crystals would have to be 6 meters long, which is impractical. With the length of crystals in the detector, a little under half of the hadrons will interact in some way in the detector.

The light produced by the shower from the incident particle is read out at the end of the crystal. There are four photodiodes, which are attached to the far end of the crystal. Four are used to make the system redundant in the event that one or more of the diodes fail.

3.2.4 Muon Chambers

The last detector that particles encounter are the chambers designed to determine if a particle is a muon. Due to their large mass compared to the electron, the muons will mainly interact in the detector gasses by ionization. Since other particles interact more in matter than the muons, the basic philosophy to determine if a particle is a muon is to put a large amount of material before the muon detectors and, if a particle makes it through to be detected, then it is a muon.

This is done first by placing the muon chamber on the outside of the detector so that a particle has to pass through the mass of the calorimeter, and then the superconducting magnet before reaching the detector. The detector is made up of three layers of active detector elements, interspersed with layers of iron. This iron is also used as the flux return for the superconducting solenoid magnet. This

detector, like the CC, is comprised of a barrel region, and two endcaps. Although the endcaps have only one layer of detectors.

Although the muon detector had proven invaluable separating muons from other particles in the CLEO III regime, it is far less useful in CLEO-c due to the lower energies available to the particles. With the energy spectrum of muons from the D mesons, very few have enough energy to penetrate deep enough in the muon chambers. There is no practical way to differential muons from other charged particles.

3.3 Event Readout and Pre-Analysis Reconstruction

The signals that a particle leaves in the detector are useless unless there is a way to read out and reconstruct the event. A large number of times when the electron and positron bunches pass through each other they either do not interact, or, if they do, do not produce an event which is worthwhile to examine. A great deal of resources are needed to write an event, so only events that contain interesting physics events are written out. Resources are taken up by the processing time to reconstruct the event and the storage to hold the event.

3.3.1 Trigger

In order to not deluge the event reconstruction and data storage, a trigger[22] is implemented so that only events of interest are recorded. The trigger takes information from various parts of the detector to determine if the event will be interesting. It looks at rough event properties without fully reconstructing the

event.

In order to handle the large amount of data and the high rate of events that are produced, the trigger has various levels the event must pass. The levels increase in complexity as the number of events examined decrease.

The triggers look at various information from two main sources, the DR and the CC. The tracking trigger is further broken down into axial and stereo components. Since the axial layers have a small number of wires, 1696, each wire is read out individually. The trigger tries to build tracks out of these hits to use for the first level of the trigger.

As there are many more wires in the stereo section, 8100, in order to expedite the output to the trigger the wires are grouped into blocks of 16 wires. The 4 x 4 block is read out to the trigger as one trigger bit, with either a hit or not. The information from the stereo and the axial trigger bits are correlated into a track, and these proto-tracks are fed into the level 1 trigger.

The other main system used for the trigger is the CC. The showers are built into shower sums, and also distributions of the energy in θ and ϕ.

The first level of the trigger, L1, looks at these tracks and showers to determine if the event should be passed onto the next level. It looks for combinations of the tracks and showers to categorize the event by predefined categories, called trigger lines. There are a number of trigger lines, each of which look for different event properties to determine if the event should be recorded. The line that the event passes is recorded so that the events can later be split into groups so that only those events of interest are examinedduring analysis. The trigger lines used for the data taking for CLEO-c are shown in Table 3.1

Table 3.1: Trigger Lines

Trigger Name	Composition	Relative Rate
Hadronic	$(N_{axial} < 1) + (N_{CBlow} < 0)$	0.41
μ pair	two back to bac stereo tracks	1.4
Barrel Babha	back to back high showers in barrel CC	1
Endcap Bhabha	back to back high showers in endcaps	0.23
electron plus track	$(N_{axial} > 0) + (N_{CBmed} > 00)$	1.48
$\tau/Radiative$	$(N_{axial} > 0) + (N_{CBmed} > 00)$	2
Two Track	$(N_{axial} > 1$	0.69
random	random 1 kHz	1

Once the event passes the trigger, all hits in the detector are read out. While this is being done the detector is disabled, to freeze the information in the detector and prevent anything further from being introduced. The time that it takes to read out the detector is "dead time," and any event occurring in this time will not be recorded. When the hits are read out they are combined into an event.

3.3.2 Pass2

The next step is to process the raw data into a usable event. This is performed by the off-line code Pass2. Pass1 is performed on the data as it is taken, and is used to examine the data as it comes out to ensure that the quality is good. Pass2 is run after the data has been stored. It performs the full reconstruction and fitting of the tracks, and the clustering of the showers.

Before this can be done the behavior of the detector must be taken out of the event. These calibration constants are used during Pass2 to remove noise from the detector, and to convert the output of the machine into physical quantities, such as the adc counts read out for a crystal in the CC versus the actual energy deposited.

Once this is done, the higher level reconstruction can take place. The tracks and showers are built, and are also matched together. The various quantities used for particle identification, such as the dE/dx and the RICH likelihoods, are also found at this time.

Another job for Pass2 is to reconstruct short lived particles, such as π^0 and K^0_S which decay before reaching the detector, so that only their daughter particles are detected. For π^0s, photons are combined to see if the resulting parent particle has the properties of a π^0. The same is done for K^0_Ss, the daughter particles are combined to see if they make a good parent. A list is created with the good parent candidates, that can be accessed when the data is analyzed.

3.4 Monte Carlo Data Simulations

Needless to say, results can easily biased if one uses the data to tune the analysis. A set of cuts can be tuned to produce a result when no signal is actually there. In order to prevent this bias and determine the correct, non biased values, a simulated data sample is needed.

Such simulated samples are called Monte Carlo [MC], and provide datasets that simulate the real data. However, they do not try and re-create each event individually, but rather do it by statistical means. Therefore instead of saying

that this particular event will have a certain decay in it, such as $D \to K^0_L\pi$, the simulation knows that a certain percent of the time a D will decay into $K^0_L\pi$, and randomly determines if this D decays to that mode or another one. Similarly, the properties of each decay and particle are taken from distributions which are entered into the MC, and reflect reality as much as possible.

There are additional reasons that a simulated sample is useful for performing analysis. In a MC sample, it is possible to "look behind the curtain" to see what the decay was for an event, and all of the properties of each particle. This is particularly useful for separating out the events that pass through the cuts for an analysis into signal and background. The background can be split into the different types, so that each can be examined individually. This is useful because when the cause of a background is known it may be possible to tailor a specific set of cuts to eliminate these background events as all of the properties of the decay are known.

The only limit on the quantity of MC generated is how much computer time can be obtained. As such, very large samples can be obtained; for this analysis the volume of MC is 10 times the size of the data set. This large MC set allows a study of properties that would not have enough statistics to be studied in the data.

Since in MC the true values of the samples are known, the numbers needed to perform this analysis can are avaible only in MC. As one example, the number of signal events measured in data is not the actual number of events in the data sample. There are background events that make it through the cuts and need to be subtracted out. Also, the analysis is not 100% efficient, and as such there is some scale factor that needs to be accounted for, given that a number of signal events will not make it through the cuts. These numbers cannot be obtained in the

data sample, but can be in MC, where the truth of the event can be examined. As such these numbers can be found within the bounds of the quality of the original information used to simulate the event.

The creation of the MC files is done in stages. The first stage involves the physics of the decay. This is accomplished by the simulation code EVTGen[16]. It simulates the electron - positron collision and subsequent primary decays of the particles. It takes as inputs the initial conditions of the collision: the beam energy, beam spread, and the crossing angle. From these it uses a decay file that gives the probability of each decay possibility of a particle to determine how it decays. For the $\psi(3770)$ regime, the electron and positron annihilate, and form a virtual photon, which decays to a $\psi(3770)$. This then decays into a $D\overline{D}$ pair, each of which is then decayed via the decay input file, and if any of the daughters are short lived, they too are decayed according to the listed decay mode probabilities.

The end product of EVTGen is a set of 4 momenta for each particle. This information is generic to the decay, has no information about the detector, and does not reflect the data that comes out of the detector, which consists of hits on tracks, shower position and energy, and the other detector readouts. The next piece of simulation code GEANT[23] takes the clean EVTGen particles and runs them through the detector. It simulates the interactions of the particle in the detector, such as material interactions or bremmstrahlung radiation. It then propagates the particles through the detector and simulates the responses of each subdetector to the particle. Now the simulated detector responses can be put into a file in much the same manner that the data is written out from the detector.

There is one last step that GEANT performs, and that is putting the real world aspects of the detector into the data. This includes: smearing by the resolution,

efficiencies, and noise from the detector. The noise is obtained from data taken when an event is not occurring. This noise is merged into the MC event. All of componants are measured run by run, so when the MC in made, each run has a specific set of constants that are used to generate the MC.

After the MC files are produced, they produce a raw data file with the same outputs as the ones from data. The only difference is that in addition to all of the reconstruction information, there is a "truth table", which gives the information from EVTGen, thus enabling the original particle properties to be compared to the detector output. The MC is then run through the same processing code used in Pass2 of the data. Therefore the MC data set can now be analyzed the same as data.

The MC used for this analysis is the generic $D\overline{D}$ sample. This means that the D's are allowed to decay randomly using the best current knowledge of the branching ratios of the the different decay modes. This is just one way in which the MC file can be generated. MC for a spicific signal can also be made. For these files, at least one of the D's is forced to decay to one specific mode. In this manner a sample with only the events of interest can be obtained. Since the decay for this analysis has a high enough branching ratio, there are enough signal events in the generic sample to study. A signal sample is obtained by looking at the generated truth table to determine if the event is a signal event.

Chapter 4

Method of Analysis

4.1 General Method

This analysis follows the general method of previous neutrino reconstruction analyses. A D meson is tagged[28] on one side of the event. The variables used to obtain the quality of the tag are the beam constrained mass, M_{bc} and delta E, ΔE:

$$M_{bc} = \sqrt{E_{beam}^2 + \overrightarrow{P}_D^2} \tag{4.1}$$

$$\Delta E = E_{beam} - E_D. \tag{4.2}$$

The 4-momentum of the tracks and unmatched showers not used to construct the tagged D are summed. The identification of each track proceeds in a conditional chain manner. First, the Rochester electron identification[ReID] is attempted. If it fails, the combined likelihood composed of the dE/dx and RICH information is used to attempt to identify the particle as a kaon. A particle that fails both identifications is assigned to be a pion. With the lack of muon id, all muons will therefore be treated as pions for the reconstruction.

The missing 4-momentum is then obtained via:

$$(E, \overrightarrow{P})_{miss} = (E, \overrightarrow{P})_{beam} - (E, \overrightarrow{P})_{visible} \tag{4.3}$$

$$(E, \overrightarrow{P})_{visible} = (E, \overrightarrow{P})_{D_{tagged}} + (E, \overrightarrow{P})_{tracks} + (E, \overrightarrow{P})_{showers} \tag{4.4}$$

For events containing only a neutrino as a source of missing momentum, the missing 4-momentum will be equal to the 4-momentum of the neutrino.

Lastly, a series of cuts are implemented to eliminate those events whose properties do not correspond to those of a neutrino-containing event. First, it is required that the tagged D is appropriate to use; second, there are cuts to eliminate badly reconstructed events; third is a cut to remove events with K_L^0, as these can fake the properties of a neutrino containing event. Last is a cut to separate the reconstructed neutrino events out by their position in the E_{Miss} vs. $Mass^2_{Miss}$ plot.

The number of events containing a neutrino is then measured, background subtracted and a correction is applied for reconstruction efficiency. This number is then divided by the number of D mesons in the sample to get the branching ratio.

4.2 Data Sets Used

Table 4.1: Luminosity

Dataset	Data pb^{-1}	MC pb^{-1}
31	21.5	229.6
32	32.4	329.4
33	10.3	65.7
35	52.0	1140
36	70.7	707
Total	186.9	2471.7

Datasets 31, 32, 33, 35, and 36, and the corresponding MC generated files were utilized for this analysis. The analysis code was run over the tagged samples. The luminosity by dataset is contained in Table 4.1.

4.3 Cuts

4.3.1 Good Tag Cuts

M_{bc} and ΔE

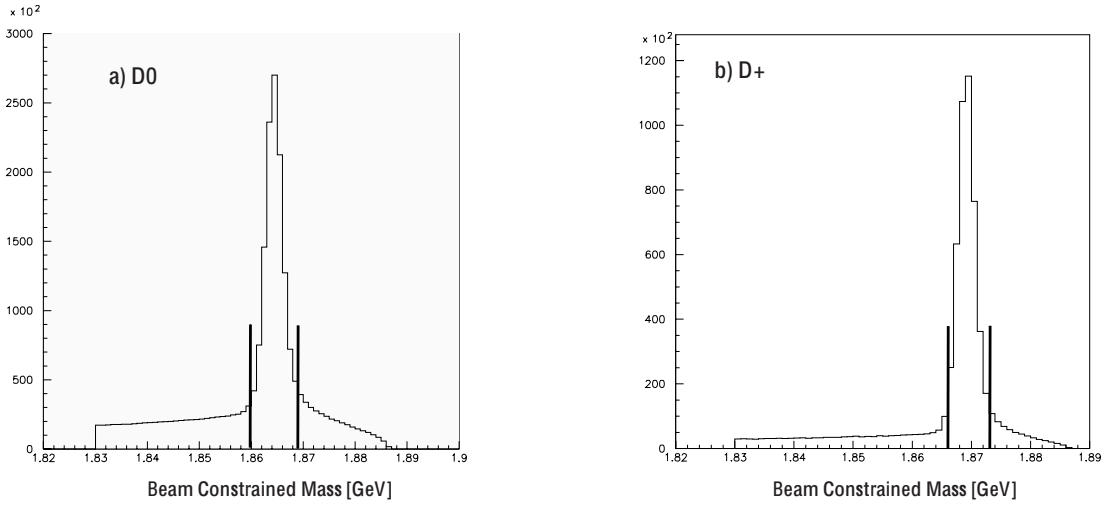

Figure 4.1: The M_{bc} for a) D^0 and b) D^+ in MC. The cut window is marked on the plot.

The first set of cuts is used to obtain a clean sample of $D\bar{D}$ pairs. A window in ΔE, Figure 4.2, between -0.02 and 0.02 GeV is used to eliminate any non-D events that happen to fall in the wider window used during tagging. The other variable used to clean up the tag sample is the beam constrained mass, shown in Figure 4.1. Windows of 1.86 GeV to 1.869 GeV for D^0 and 1.866 GeV to 1.873

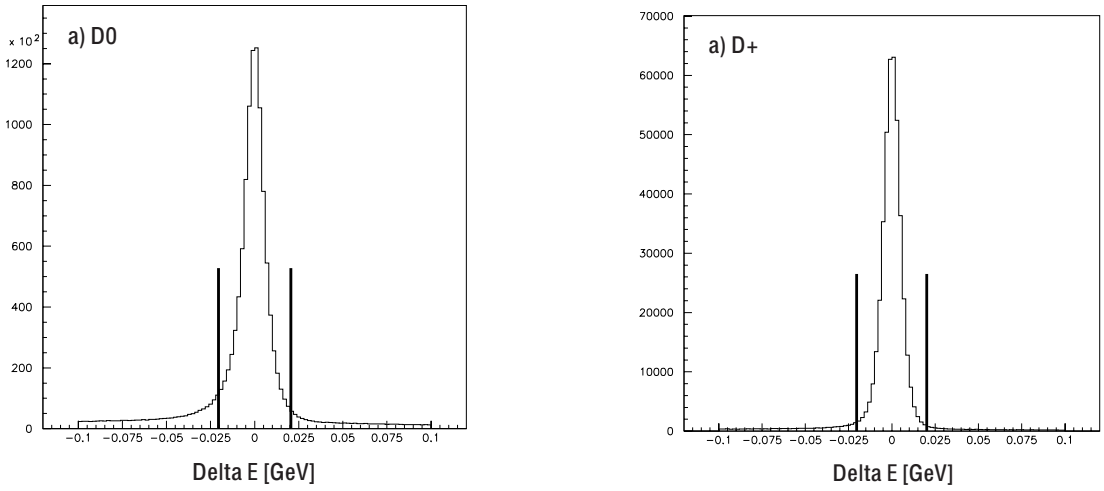

Figure 4.2: The ΔE for a) D^0 and b) D^+ in MC. The cut window is marked on the plot.

for $D^{\pm}$ are used. These values were selected to be at the values where the peak in M_{bc} intersects the background level.

Number of Tags Per Event

During tagging some events will have more than one tag assigned, due to misidentification of particles. There will be a tag present for this mis-identification along with the correct tag. These extra tags will cause an incorrect number in the denominator when calculating the Branching Ratio. An attempt was made to use the presence of particle identification to eliminate the incorrect tags, but due to the limited geometric acceptance of the RICH detector, this method would necessarily also eliminate a large number of good tags also. Examining the number of tags in each event, illustrated in Figure 4.3, it is apparent that the vast majority of events have only one tag. Thus, eliminating all events with more than one tag does not remove a significant number of events. Table 4.2 shows that after this cut has been performed there are very few misidentified daughter particles remaining.

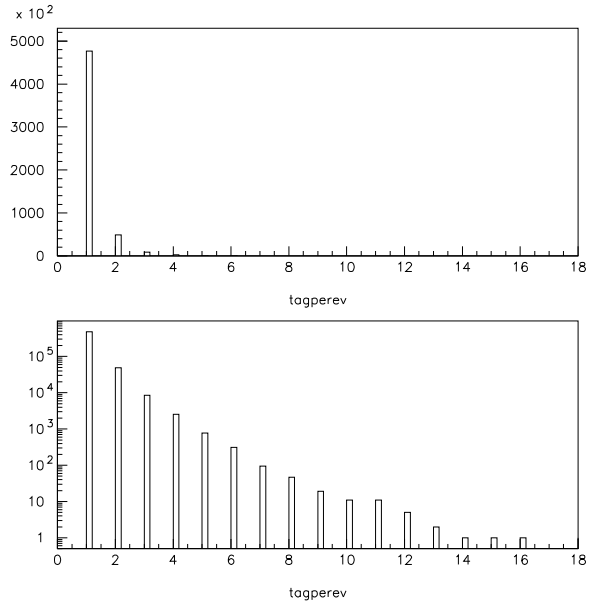

Figure 4.3: The number of tags Per Event, Linear - top and Log Scale - bottom in MC

4.3.2 Clean Event Cuts

The clean event cuts are used to confirm that the reconstruction of the missing 4-momentum is performed correctly. If it has been determined that it was not, then the event will be dropped. Table 4.3 lists the cuts in this category.

The first set is used to confirm that each track is well reconstructed, as shown in Table 4.4. The cuts follow the CLEO III Rare B analysis[24] track quality cuts. The only distinction is here the χ^2 cut on the track fitting is tightened to eliminate some badly reconstructed tracks. The variables used for track quality are as follows: hitfraction - fraction of layers with hits versus how many are predicted based upon the fit, d0 - distance of closest approach to the interaction point, z0 - distance of closest approach to the interaction point (IP) in the z direction, and the errors on the fit for z0 and cotθ.

Table 4.2: Number of D daughters that are misidentified when using Good Tag Cuts in MC

Particle MisIDed	Number of Tags with misID	Percent in MC
Kaon	127	0.11 %
Pion	576	0.53 %
Total number of tags	109070	

Table 4.3: Cuts used to ensure the reconstruction was done correctly

Variable	Value
tracks	track quality and Trkman
number of tracks lost to quality	0
showers	splitoff approved
missing momentum angle	$\cos\theta < 0.94$
total charge of event	0

When a track does not possess sufficient transverse momentum, the solenoid's magnetic field will bend it in a full circle giving the appearance that there are two tracks in the DR as opposed to one. A processor included during the running of the analysis, Trkman[25], attempts to determine the correct leg of the curler to use.

In a manner similar to Trkman, Splitoff[26] determines if a shower should be included in the visible momentum sum. A splitoff shower is detached from the main

Table 4.4: Track Quality Cuts

Variable	Value
track fit	valid
fitAbort	false
χ^2	< 20
Reconstructionhitfraction	< 1.2
hitfraction	> 0.5
d0	< 0.02
z0	< 0.1
costheta	< 0.95
error cottheta	< 0.3
error z0	< 0.5
trkman	approved

energy deposition from a particle in the calorimeter. As its energy has already been accounted for in the sum from reconstructing the track, the shower's energy should not be included.

If the missing momentum vector falls outside of the detector volume, essentially pointing down the beampipe, it could be caused by a normally visible particle which did not pass through the detector. It is usually impossible to differentiate these types of events from those with neutrinos, and because of this fact these events are eliminated.

The last cut in this group requires that the total charge of the event be equal

to zero. This is performed as a check to ensure that all of the charged particles in the event have been accounted for in the reconstruction.

4.3.3 K_L^0 Suppression Cut

K_L^0 as Background

The largest source of background for the neutrino containing events are those that have a K_L^0 in them. This is due to the fact that since there is no hadronic calorimeter, they can escape the detector without depositing all of their energy, making it impossible to fully reconstruct the event. A study of the properties of the K_L^0 in the detector was undertaken in data to ensure that the K_L^0 is simulated correctly in the MC.

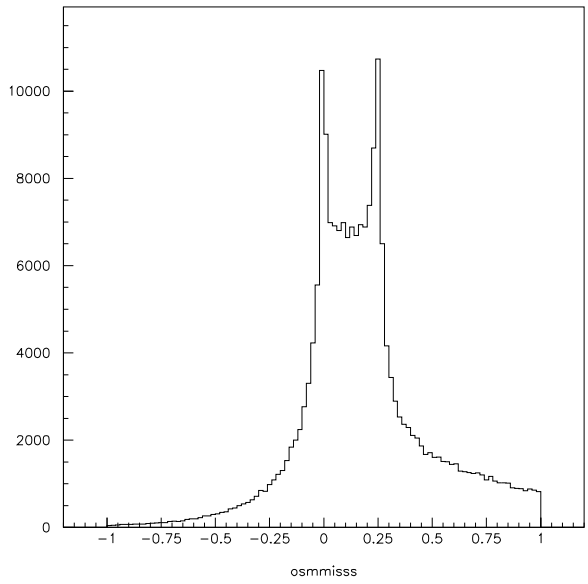

Figure 4.4: The $Mass^2_{Miss}$ of events that contain a K_L^0 in MC. The peak at zero are non K_L^0 that deposit all of their energy in the detector, while the peak at 0.25GeV are non-interacting K_L^0.

Examining Figure 4.4, a plot of the $Mass^2_{Miss}$ for events containing a K^0_L, shows that a K^0_L has three possible ways in which to interact in the detector. Since the crystal calorimeter is one nuclear interaction length, approximately half of the K^0_L will interact and deposit some fraction of their energy in the calorimeter. This leads to three possibilities of how the K^0_L will interact in the detector.

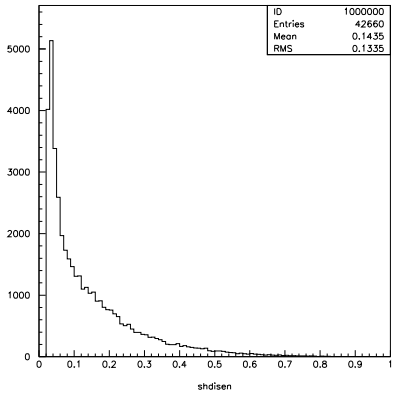

Figure 4.5: The energy of a shower produced by a K^0_L in MC

- **Non - Interacting** These K^0_L pass through the detector without interacting, depositing no energy in the calorimeter. The event has missing energy equal to the energy of the K^0_L, and a $Mass^2_{Miss}$ equal to the mass of the K^0_L squared, .250 GeV^2. These events can be easily eliminated by the requirement that $Mass^2_{Miss}$ is close to zero, as it should be for a neutrino.

- **Full Energy Deposition** These K^0_L fully hadronize in the detector, leaving all of their energy in the calorimeter. On the E_{Miss} vs. $Mass^2_{Miss}$ plot these events, if there is no other source of missing energy of momentum, will appear at the origin, as they will be fully reconstructed. These events can be eliminated along with the fully reconstructed hadronic events.

- **Partial Energy Deposition** The events pose more of a difficulty in being

separated from events containing a neutrino because the K_L^0 leaves only a fraction of its energy in the calorimeter. Figure 4.5 shows the distribution of energy deposited by such a K_L^0. These events can fall anywhere between zero and $M_{k_L}^2$, which can put them in the signal region used to select neutrino containing events. There are large tails in both directions in this plot, due to misreconstruction errors in other parts of the event.

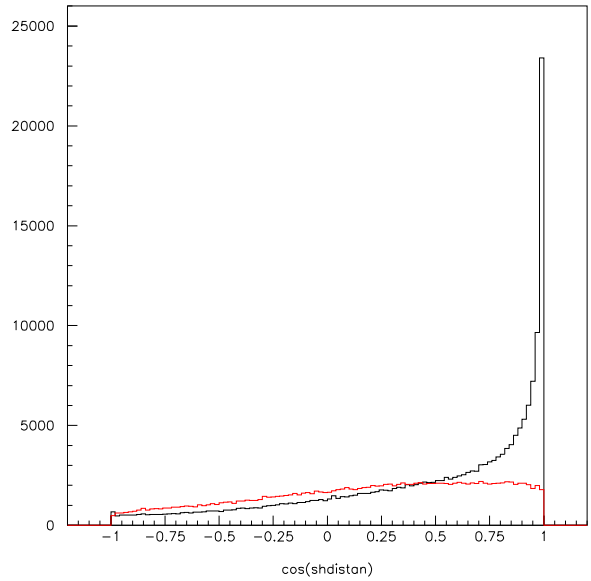

Figure 4.6: The closest shower angle for signal and background: solid = background: dashed = signal in MC

K_L^0 Shower Cut

A large part of the background to our signal is composed of events containing a K_L^0. It is not possible to use the shower from a K_L^0 to obtain the full energy of the K_L^0, and therefore it is not possible to get the full reconstruction for the event. However, the position of the shower in relation to the direction of the missing momentum vector can be used to eliminated these events. If the shower

is produced from a K_L^0, it will be produced with a small angle with respect to the missing momentum vector. Utilizing this fact, a cut can be made on the angle of the closest shower to the missing momentum vector. Figure 4.6 plots this variable for MC events with a K_L^0, and those with a neutrino. The K_L^0 events peak strongly at small angles compared to the flat distribution for signal events. This cut can then be used to help eliminate the events with interacting K_L^0. If there are no unmatched showers in the event, which occurs for 70 percent of signal events, then this cut is not performed. There is a minimum shower energy cut at 25MeV performed by Splitoff.

This cut is in principle dependent on the proper simulation of the interactions of the K_L^0 in the detector. To double check that the MC does this in a correct manner, a study of $D \to K_L\pi$ in data was undertaken to compare the properties of the K_L^0 in data versus MC.

4.3.4 Neutrino-Like Cuts

Table 4.5: Cuts used to separate out events that contain a neutrino.

Variable	Value
missing energy	> 0
missing momentum	> 100 MeV
number of tracks	> 0

The last grouping of cuts separates neutrino like from non-neutrino like events, since it is not possible to simply tag the neutrino. The first cut requires that

the missing energy be greater than zero. Second, is a cut on missing momentum, requiring it to be greater than 100MeV. This eliminated the fully reconstructed hadronic events. Lastly, there must be at least one charged track in the event to account for the charged lepton which will be produced along with the neutrino.

V cut

The last cut is based upon the requirement that for a neutrino:

$$Mass^2_{Miss} = E^2_{miss} - P^2_{miss} = 0 \tag{4.5}$$

However, due to the increase in resolution in $Mass^2_{Miss}$ with increased E_{Miss} the cut must be widened at higher E_{Miss}, giving a cut of constant fractional error on the $Mass^2_{Miss}$. The $Mass^2_{Miss}$ can be factorized into $(E+P)(E-P)$, with the subtractive term containing the information, and the additive term contributing smearing with a strength $\propto E$.

The equation for the cut is:

$$E_{Miss} > \pm 11 * Mass^2_{Miss} + 0.1 \tag{4.6}$$

4.4 MC Results

The plot of E_{Miss} vs. $Mass^2_{Miss}$ yields a large amount of information about the analysis. The plot gives information about the behavior of different types of events, and indicates how it would be possible to eliminate various types of backgrounds. Additionally, the plot can serve as a check that the reconstruction has been done correctly, as different problems will show up as groupings of events in anomalous locations.

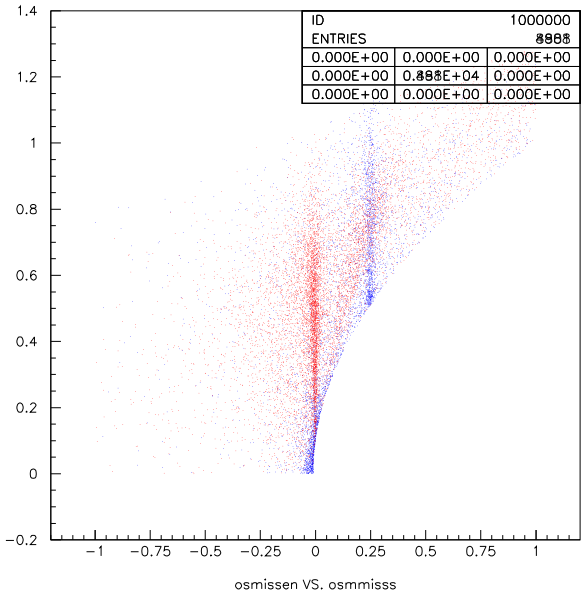

Figure 4.7: E_{Miss} vs $Mass^2_{Miss}$ MC

4.4.1 General Features of E_{Miss} vs. $Mass^2_{Miss}$ Plot

Figure 4.7 has all cuts except for the V cut, and is plotted for the Monte Carlo for datasets 31-33, as some of the features on the plot are from problems that were subsequently fixed. Events plotted in blue do not contain a neutrino, while the signal events are in red.

The first and most important feature of this plot is the vertical line of signal events at $Mass^2_{Miss}$ = zero. These are the well reconstructed neutrino containing events. They have a missing energy equal to the energy of the neutrino, and, as is appropriate for mass-less neutrinos, a $Mass^2_{Miss}$ of zero. Also visible is the increase in resolution with higher E_{Miss}.

The next salient feature is the vertical line of blue background events at 0.250 GeV^2. These are events containing a non-interacting K^0_L. Like a neutrino con-

taining event, the missing energy will be that of the K_L^0, but given that the K_L^0 is massive the $Mass^2_{Miss}$ will not be zero, but rather peak at a value of the mass of the K_L^0. These events are well separated from the neutrino containing events and can be easily eliminated with the V cut.

The grouping of blue background events at the origin are hadronic events. They are fully reconstructed and therefore have no missing energy or momentum. They encroach into the signal region due to resolution or errors in the reconstruction. The last feature is the curved boundary line on the high side in $Mass^2_{Miss}$. The explanation for this is simple - at a fixed value of E_{Miss}, since $Mass^2_{Miss} = E^2_{miss} - P^2_{miss}$, you get a maximum E_{Miss} when $P^2_{miss} = 0$ and therefore, this cutoff line is simply the curve E^2_{miss} vs. E_{miss}.

Misidentification of Particles

One example of how the the plot of E_{Miss} vs. $Mass^2_{Miss}$ can be used to identify errors in the reconstruction of the event is how it was used to correct a problem in the particle identification undertaken during the signal side reconstruction.

A faint line of signal events is visible in Figure 4.7 lying just to the right of the vertical line of correctly reconstructed signal events, with a positive slope. It is first postulated that it could be due to slow pions that do not get included in the reconstruction. However, an examination of the decay tree from Monte Carlo showed that slow pions were not present in the events that fell into this diagonal line.

Another potential cause of events being mis-reconstructed in this manner would be if a kaon were mis-identified as a pion. Using this information, an error was

found in the analysis code, where if a particle did not have RICH information, instead of using the dE/dx to attempt a particle identification, it was automatically treated as a pion. This mass difference used for reconstruction accounts for the shift of the events in the E_{Miss} vs. $Mass^2_{Miss}$ plot.

With the reconstruction code fixed, it is informative to examine how well the different particle id's work. Figure 4.8 shows the quality of each main type of particle id. The top plot is for MC tagged Kaon, the middle for pions, and the bottom is for electrons. The bin that a track is placed in indicated how it was identified for the event reconstruction. Bin one is a track identified as a kaon, two for a pion, and three for an electron.

The majority of kaons are correctly identified, as well as pions. The reconstruction efficiency is worse for electrons for two main reasons: 1) there is a very low efficiency for tracks under 200MeV, and 2) there is a lower efficiency in the dE/dx crossover region.

4.4.2 Left Side Tail in $Mass^2_{Miss}$

Examining the E_{Miss} vs. $Mass^2_{Miss}$ plot in MC for signal events, Figure 4.7 makes it apparent that there is an excess of events on the negative side of $Mass^2_{Miss}$. This can be seen more clearly in Figure 4.9, which is the plot of $Mass^2_{Miss}$ for signal events in MC.

A comparison of data and MC was undertaken to ensure that the excess of events on the left side of the $Mass^2_{Miss}$ plot is not due to a problem with the simulation. Figure 4.10 shows that this excess of events exists for both data and MC, indicating that the problem is with the analysis, and not a difference between

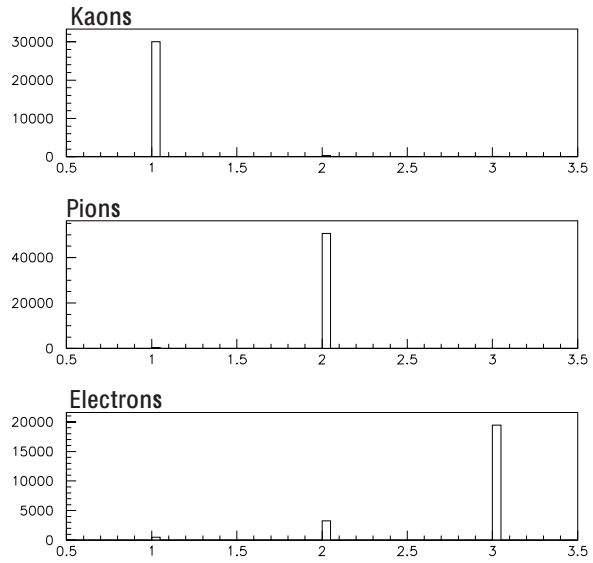

Figure 4.8: How well each type of identification works in MC. The top plot is for MD identified Kaon, the middle pions, and the bottom electrons. Bin one contains particles identified by the analysis code as a kaon, two defaulted as a pion, and three identified as an electron.

data and MC.

Properties of events in the left tail region were examined and compared to those that are correctly reconstructed at $Mass^2_{Miss} = 0$. Properties examined include: which run the event was from, what number event it was in the run, which tagged D was used, which semileptonic decay mode was present, and the number of tracks. All of these properties exhibited showed no difference between left-side and normal events.

The only plots that show any difference are the missing momentum angle and the number of showers in the event [Figure 4.11]. The first plot shows the cos-theta of the missing momentum vector. The solid line is for signal events, and the dashed line shows the distribution for left-side events. The well reconstructed events have

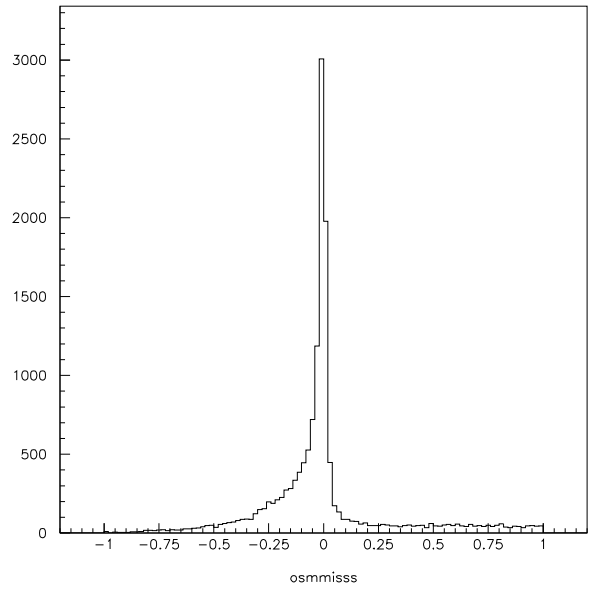

Figure 4.9: The $Mass^2_{Miss}$ for signal events in MC with a high tail on the left side of the plot.

a flat distribution while the left events are biased towards negative z. The other difference is that the multiplicity of showers in the event is higher for left events. The left events have at least one shower.

Isolating left events in which there is only one photon ensures that if the photon is causing the shift that can be isolated and studied. A plot of the cosθ of the photon vs. the cosθ of the missing momentum vector, Figure 4.12, shows that the photon and momentum vector are anti-correlated, and additionally that the distributions peak at the forward and backward directions.

One explanation which accounts for all of the information obtained, is that the photon is adding extra energy to the 4-momentum sum. If extra energy is added to the sum on one direction, it will cause the missing energy vector to appear in the opposite direction. This would occur if the shower should have been excluded by Splitoff, but was passed in error. The result would be the shower being double

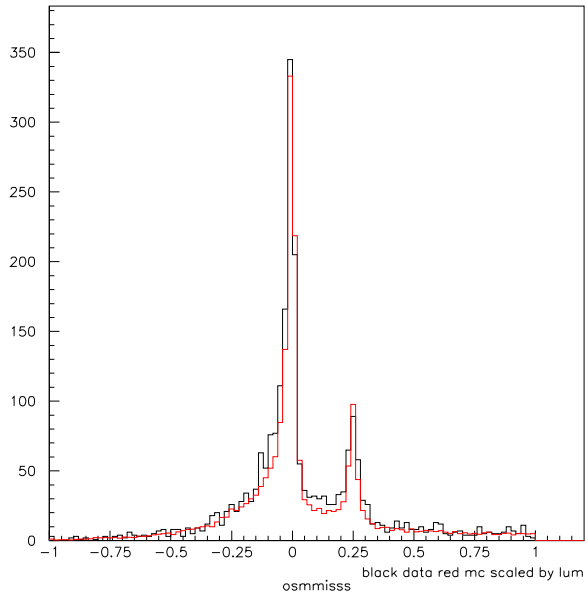

Figure 4.10: The $Mass^2_{Miss}$ plotted for data - solid, and scaled MC - dashed

counted.

Whether these photons are being double counted can be tested by subtracting them out from the 4-momentum sum. Again, only looking at events containing a single photon assures that the correct photon will be subtracted. Figure 4.13 contains, on the left, a plot of the generated E_{Miss} minus the reconstructed for left side events before and after the photon is subtracted out. After the photon subtraction is performed, the peak is centered at zero. The right plot is $Mass^2_{Miss}$ before and after photon subtraction. Taking out the photon from the 4-momentum sum puts these events at $Mass^2_{Miss} = 0$

Additional proof that the photon is being double counted is the location of these events on the E_{Miss} vs. $Mass^2_{Miss}$ plot. As shown in Figure 4.14, when the photon is subtracted out, the events move from the left side into the signal region.

One possibility for the double counted photons is that they are produced from

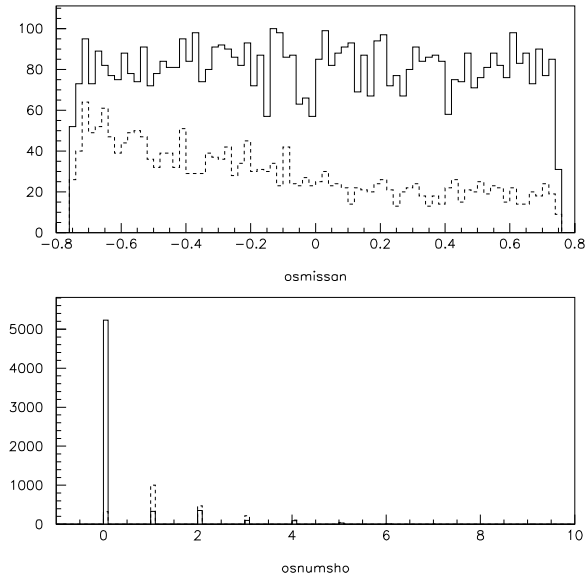

Figure 4.11: Top: Missing angle, Bottom: Number of Showers, for events in the signal box,(solid) and those on the left side, (dashed) in MC

material interactions in the detector. If they are produced after the majority of the drift chamber has been traversed, the momentum contained in the photon has already been accounted for in the reconstruction of the track. Figure 4.15 shows the radius of production for photons in the left events. The majority of the photons are produced inside of the beam pipe. Therefore, a different mechanism must be responsible for the double counting.

Splitoff

The most obvious culprit when showers are mistakenly included in the reconstruction is Splitoff. Splitoff filters out the showers produced by charged tracks, that are disconnected from the main shower. The 4-momentum of the showers have already been included in the visible sum when the track is added, and therefore if these showers are not eliminated by the code they would be double counted and

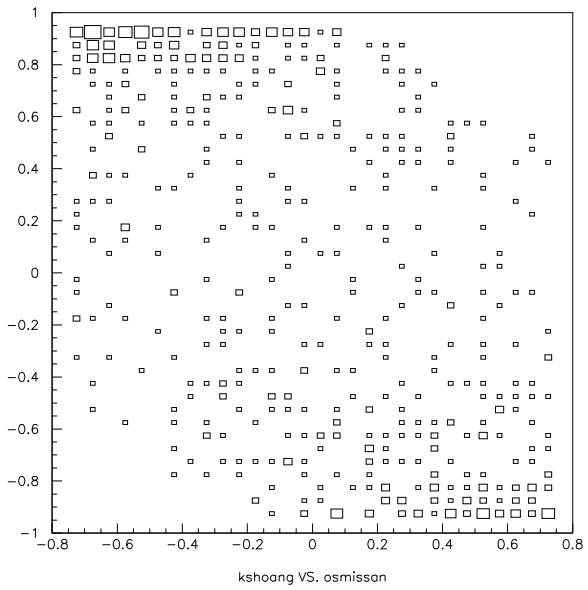

Figure 4.12: Shower angle vs. Missing Momentum Angle for left-side events MC

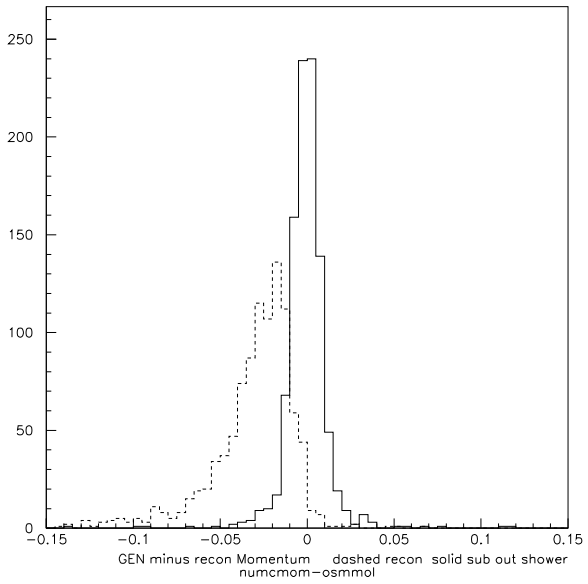

Figure 4.13: $Mass^2_{Miss}$ for left events before, (dashed), and after, (solid), the photon is subtracted.

could cause the left shift observed for these events.

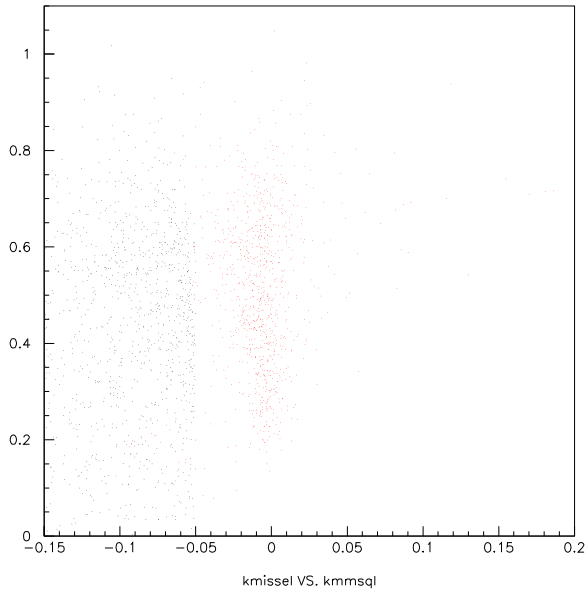

Figure 4.14: E_{Miss} vs. $Mass^2_{Miss}$ for events in the left side region, on the left of the plot, and the same events after the photon is subtracted out, those that appear in the center, in MC

Splitoff uses a neural net algorithm to determine if a shower originates from a photon or is a splitoff of a shower from a track. It determines a variable from -1 to 1, with -1 being a photon-like shower, and 1 being splitoff-like. Figure 4.16 shows the discriminatory variable that is the output from Splitoff. A large number of showers have an output of -5, which indicates that there was a problem in the neural net calculation. When this occurs the shower is automatically passed. Putting this informmation together with the fact that these showers are at large angles in the detector explains what is happening. For part of its calculation, Splitoff takes sums over three rows and three columns of crystals. If the shower falls on the border of one of the sections of the detector, the sums fail, and Splitoff will pass the shower.

This problem has been substantially addresed by implementing the following

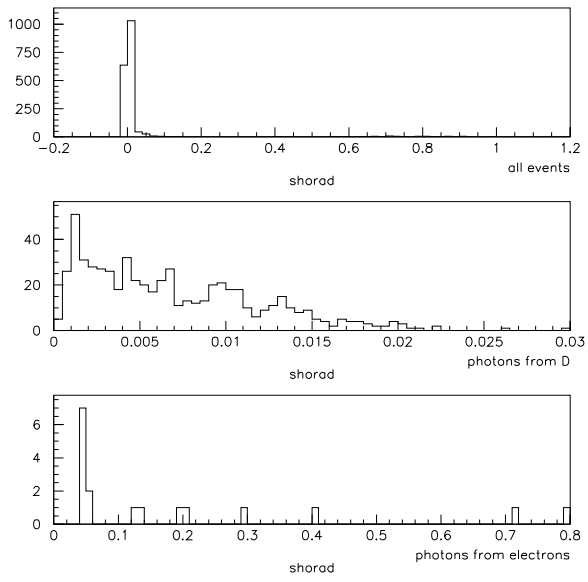

Figure 4.15: Radius of production for photons from events in the left-side region MC, Top all photons, Middle from D, Bottom from electron

measures:

- **Bad Shower Cut** The bad shower cut substantially eliminates events that contain a shower with $|cos\theta| > 0.8$, unless that shower is used to make a π^0. This cut was the first attempt to resolve the problem of extra showers.

- **Outer rings** The two outermost rings on either side of the detector, the ones closest to the beam pipe, have a large number of showers caused by beam gas and other beam-related effects. Any shower in these 4 rings is discarded from the visible energy sum.

- **Retuned Splitoff** The version of Splitoff used previously was tuned for CLEO III showers, and made no attempt to eliminate the showers at the ends of detectors. Splitoff was then re-tuned specifically for CLEO-c data. The re-tuned version excludes showers in the overlap region of the calorimeter.

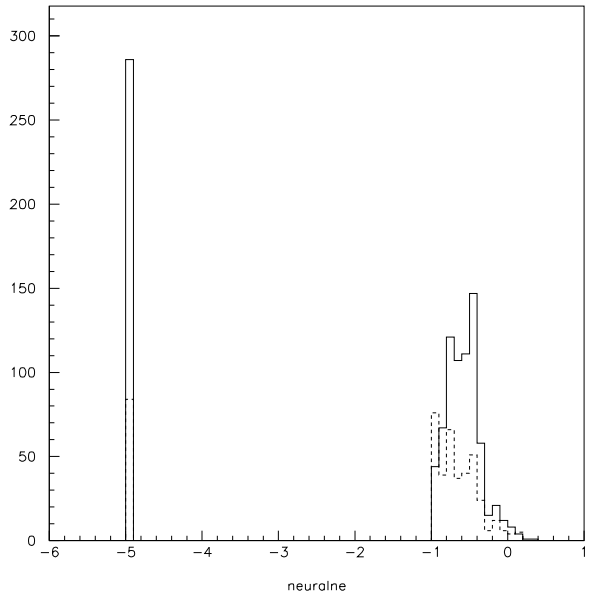

Figure 4.16: The Neutral Net Output for shower in the left-side tail, solid, and signal region, dashed. MC

This not only eliminates the problem of events being shifted left, it also more than doubles the overall efficiency for reconstruction since it eliminates only the shower and not the entire event.

It is worth examining how the newly tuned splitoff affects the discriminatory variables for this analysis. The $Mass^2_{Miss}$ for signal events in MC is plotted in Figure 4.17. Events analyzed with the old splitoff are plotted in black, while events that used the new splitoff are plotted in red. As expected for events where the only missing 4-momentum comes from a neutrino, both peaks are centered at zero.

The two major changes are the number of events in the peak and the tails. Events that would be eliminated by the bad shower cut are now included, since the shower in the overlap region that would trigger the cut are eliminated by splitoff

before the event reaches the reconstruction. Therefore more events now pass the cuts used for this analysis. More importantly, the rise in the left side tail has been greatly reduced due to the reduction of extra showers. There is also a small rise in the right side tail. This is due to the 5% of crossover region showers that are from real photons, which are now removed.

The missing energy is plotted in Figure 4.18. This plot is made with all of the cuts, including the V cut, which eliminated events outside of a narrow window around $Mass^2_{Miss} = 0$. This cut eliminates the differences in the badly reconstructed tails as these events have been eliminated. The difference that does show up is the number of events that pass the cut. The new splitoff, in addition to the previous well-reconstructed events, now adds the events that had been eliminated due to the bad shower cut, giving it a much higher reconstruction efficiency. The spectrum shape has not changed overall.

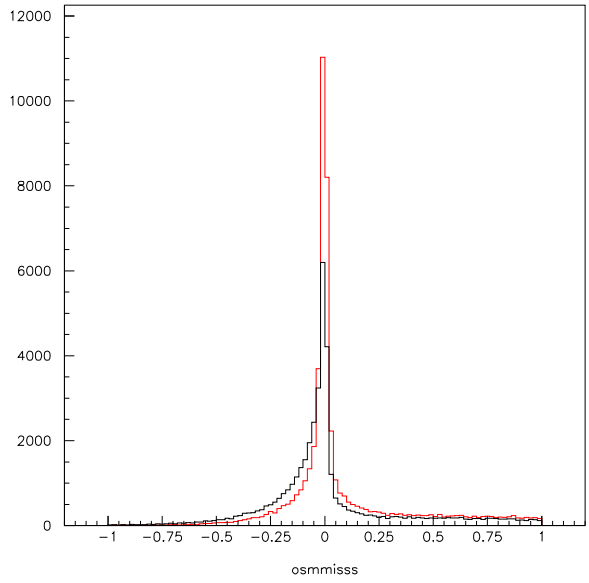

Figure 4.17: The $Mass^2_{Miss}$ for old - (solid), and retuned - (dashed) Splitoff.

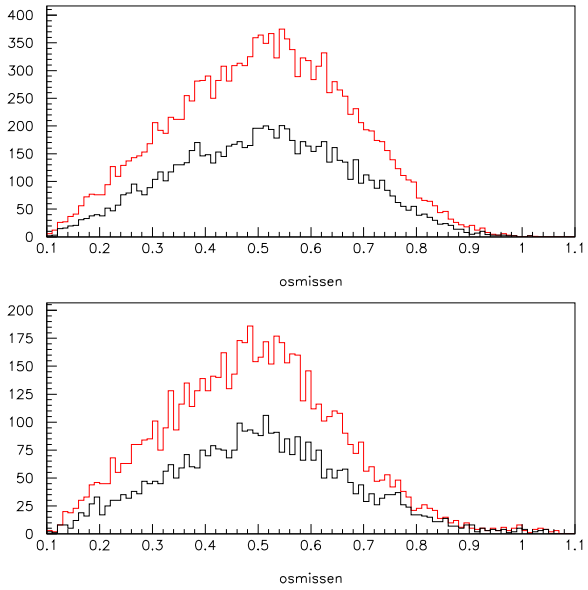

Figure 4.18: E_{Miss} for old - (solid), and retuned - (dashed) Splitoff. The top plot is for D^0, with the bottom plotting D^+.

Finally, after implementing the V-cut, the spectrum can be plotted. After the left-side event, and bad particle identification code fixes, it is valuable to look at the the E_{Miss} vs $Mass^2_{Miss}$ plot again (Figure 4.19). This plot is now considerably cleaner, with the left side tail removed, and the diagonal line of misidentified particles corrected.

4.5 MC Energy and Momentum Plots

With all of the cuts implemented, the spectra for missing energy are plotted in Figure 4.20 for neutral and Figure 4.21 for charged D in MC. For both plots, the black line is all of the events that pass the cuts. The red line is neutrino containing events, while the blue line is background.

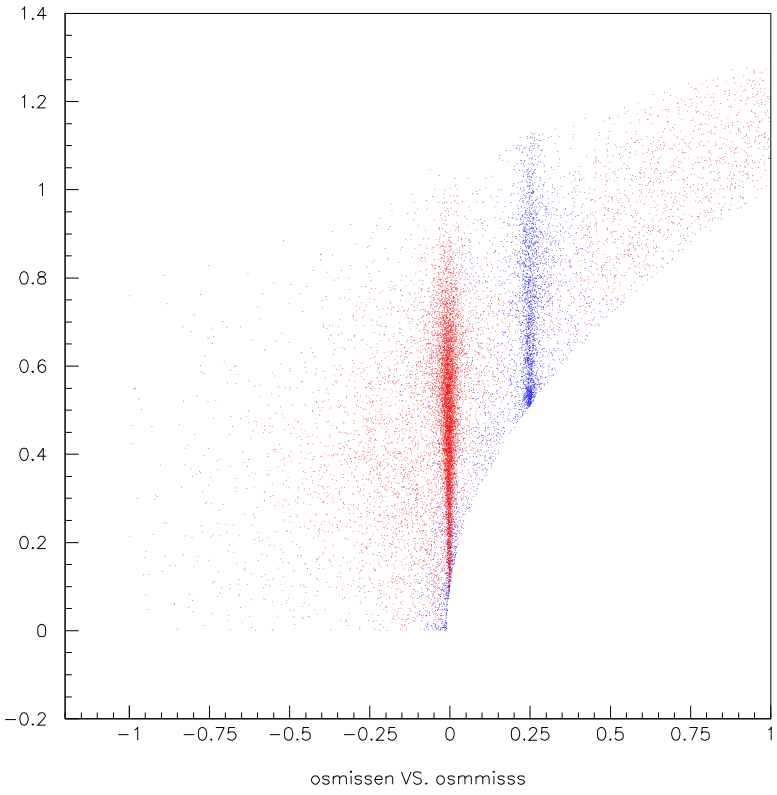

Figure 4.19: Corrected E_{Miss} vs. $Mass^2_{Miss}$ MC

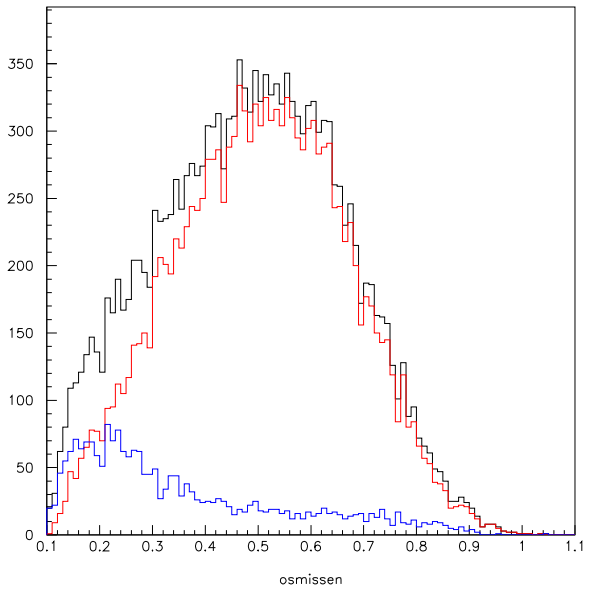

Figure 4.20: The E_{Miss} spectrum for D^0. (Solid) all events that pass the cuts, dashed are events containing neutrinos, and dotted is background MC

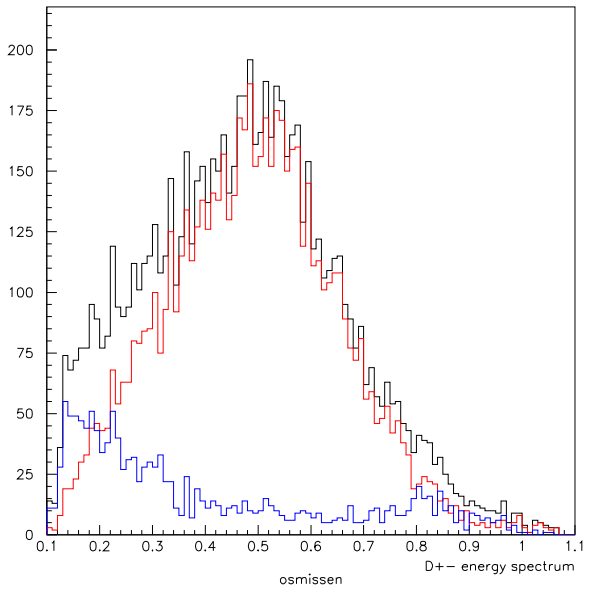

Figure 4.21: The E_{Miss} spectrum for D^+. Solid is all events that pass the cuts, dashed are events containing neutrinos, and dotted is background MC

4.5.1 High E_{Miss} Events in D^+ Decays

Examining the spectrum for charged D events shows that compared to the neutral D, there is a rise in both signal and background. These occur for different reasons, and fortunately the excess in background can be mostly eliminated.

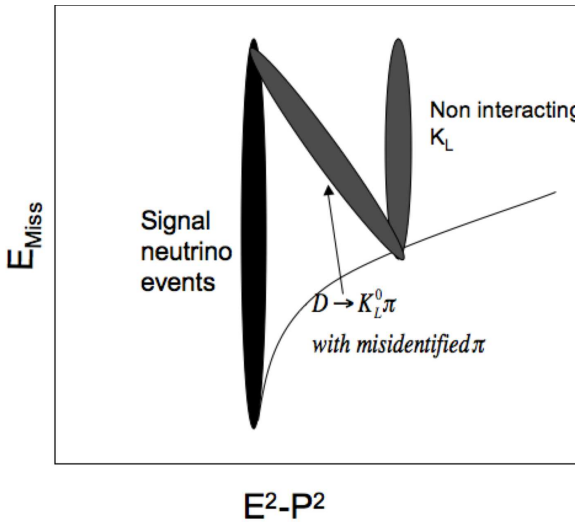

Figure 4.22: Sketch of $D^+ \rightarrow K_L\pi^+$. The diagonal line contains events where the pion is misidentified as a kaon.

Using the MC decay tree, the excess background events can be identified as $D^+ \rightarrow K_L\pi^+$. An examination of the E_{Miss} vs. $Mass^2_{Miss}$ plot helps determine what is occurring with these events. If these events were correctly reconstructed they would appear in the vertical line of K^0_L events to the right of the signal region. This can be seen in Figure 4.22. If the K^0_L deposits none of its energy in the detector, it would move down towards the origin as it deposits a greater fraction. If this were the case it would enter the signal region at low E_{Miss} since the K^0_L has deposited most of its energy, and the event is almost fully reconstructed.

Further examination of the properties of these events show that the pion is

being misidentified as a kaon. Like the misidentification of kaons previously in signal events, this will move the events from a vertical line to a diagonal one. Since the pion is now being identified as a kaon, the line will be to the left of vertical. Therefore for events that would otherwise be in the line of events where the K_L^0 leaves no energy will now be shifted left. The extra background events occur from where the diagonal line intersects our signal region at $Mass^2_{Miss} = 0$.

To eliminate these events, given that there is no shower from the K_L^0 for the closest shower cut, a new cut must be implemented. A cut on events containing a single track that is identified as a kaon will eliminate all of these events.

Since there are signal events with only one charged track, an electron or a muon, a check must be done to make sure that they are not identified as kaons. Figure 4.23 plots how electrons and muons are identified for reconstruction by the analysis code. Neither charged lepton is treated as kaon, so this is a safe cut that will not eliminate any signal events.

Figure 4.24 shows the missing energy spectrum for the charged D after this cut has been implemented. The rise in background at high E_{Miss} has been suppressed, and the peak in signal events can be examined.

The excess at high E_{Miss} in the neutral spectrum is caused by the two body decay $D \to \mu\nu$. As it is a two body decay the energy of the daughter neutrino will have a sharp peak at half of the energy of the D. Unfortunately the resolution is not good enough, and the backgrounds, now including the other signal modes, do not allow a individual measurement of this mode.

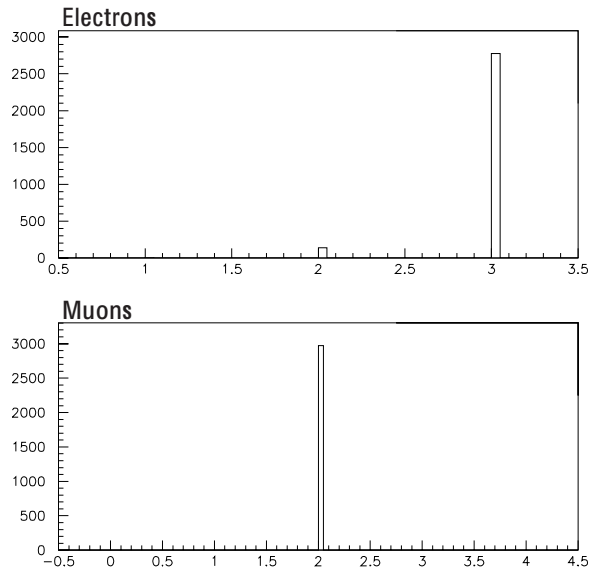

Figure 4.23: How leptons are identified. The bin indicate how the particle is identified by the reconstruction code: 1 - kaon, 2 - pion, 3 - electron.

4.6 Study of $D^{\pm} \to K_L \pi^{\pm}$

Given that events containing a K_L^0 comprise the largest background, this analysis is very dependent on how well the MC simulates K_L^0 interactions in the detector. If they are poorly simulated, the correct number of K_L^0 containing events will not appear in the MC signal region, which will in turn cause an incorrect number to be subtracted out in data. There are numerous factors that may lead to the K_L^0 being incorrectly simulated including an error with: the fraction of K_L^0 that interact in the detector, the amount of the energy the K_L^0 deposited in the detector, the position of the showers, and the number of showers produced. The shower properties are the most important because they will directly affect how the closest shower angle differs between data and MC, and can cause a systematic error. A study of the decay $D^{\pm} \to K_L \pi^{\pm}$ is undertaken in data to determine the properties of the K_L^0 in the detector, and to determine how well they are simulated in MC.

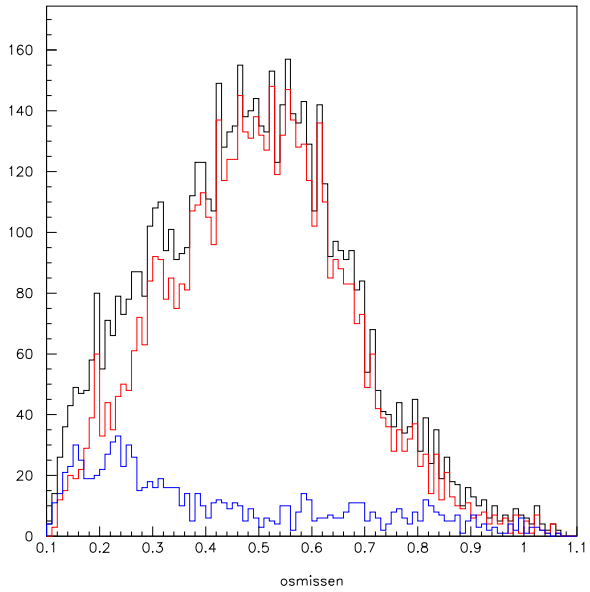

Figure 4.24: E_{Miss} for D^+, The single track cut has now been applied. MC

4.6.1 Method

The study of $D^{\pm} \to K_L \pi^{\pm}$ will be performed first in MC, and then once the method is finalized, the properties of K_L^0 in data can be studied. The method is held as close as possible to the main analysis to avoid introducing bias in the variables being studied, and to ensure that the information gained will transfer between the two.

The tagged D samples are again utilized to assure a D on the signal side. All tracks and showers used to reconstruct the D are eliminated from consideration on the signal side. The same cuts used for ΔE and M_{bc} are utilized, and the requirement that there be only one tag per event is retained. This assures a clean sample of D's.

The next requirement is that there is only one charged track, which is positively

identified as a pion, through RICH and dE/dx information. This requirement will eliminate a great deal of background, as it leaves only neutral particles for the signal side. The track is run through the electron identification as a filter. This is done because the electron ID package has a very small fake rate, while there is a measurable one for the pion ID, so before the the single charged track is tested as a pion, it is run through the electron ID as a filter.

The next cut requires that the D is decaying into two bodies. If the pion is boosted into the rest frame of the D, it will be mono-energetic if it comes from a two body decay. Figure 4.25 plots the momentum of pion in the D rest frame in which the sharp peak can be seen. Cutting on this peak will leave mostly two body decays.

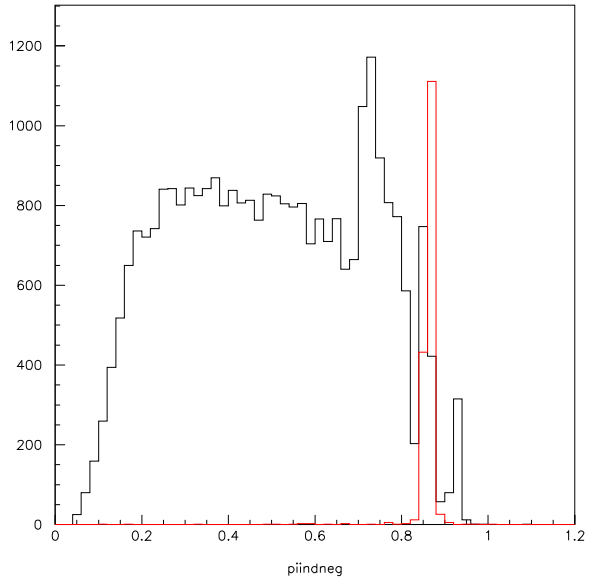

Figure 4.25: The pion momentum in D Rest Frame. Dashed = K_L^0 events. MC

While this study is interested in finding the decay $D^{\pm} \to K_L \pi^{\pm}$, the decay actually goes as:

$$D^{\pm} \to K_L^0 \pi^{\pm} \tag{4.7}$$

$$K^0 \rightarrow K_L^0 \text{ or } K_S^0 \tag{4.8}$$

Thus while we have eliminated most non-two-body decays not containing a charged pion, events that decay to a K_S still remain. These events are removed through a two stage cut. First, events are removed in which a reasonable K_S can be constructed. Given that there has already been a requirement that there be no additional tracks, the K_S can only be constructed of neutral daughters.

In the event that a "good" K_S cannot be constructed, since it decays to two π^0 particles, a cut can be made on the number of π^0 in the event to further remove K_S^0. Figure 4.26 contains the number of π^0 that can be constructed in signal and background events. The number of π^0 that can be constructed for signal events is zero for the majority of the events. An additional cut is applied on events where a π^0can be constructed.

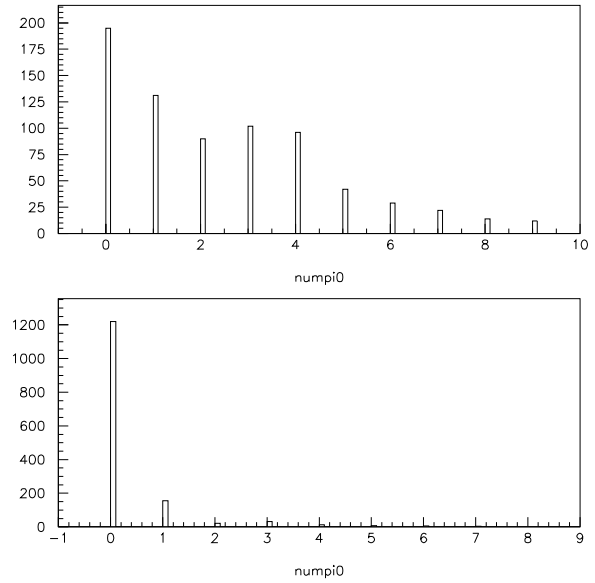

Figure 4.26: Number of π^0in Event for top: background and bottom: signal MC

This study examines the properties of the K_L^0, and specifically those of the

showers they produce. A check is performed to ensure that the elimination of events containing a π^0 does not affect the shower distribution. The multiplicity of showers in plotted in Figure 4.27 for those occurences with no π^0 cut, for the number of π^0 less than 2, which would eliminate the construct-able K_S, and for a requirement that it is not possible to construct any π^0, which covers the case where one of the daughter π^0 is not able to be constructed. Given that there is only a small difference in the plots, the tighter cut can be applied without altering the quantities that are being studied.

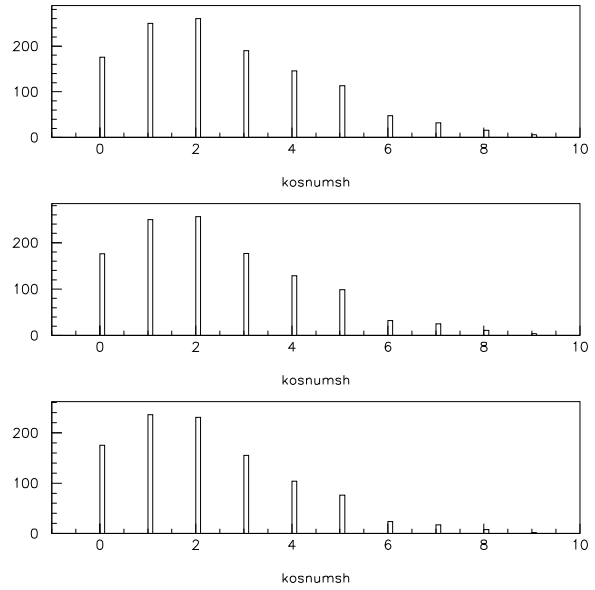

Figure 4.27: Multiplicity of Showers - Top - no π^0cut, Middle - number of $\pi^0 < 2$, Bottom - Number of $\pi^0 = 0$

This study was performed with the old version of Splitoff, as such it contains the incorrectly passed showers on the borders of the calorimeter. As before a cut is applied that if an event contains a shower whose $cos\theta$ is greater than 0.8, and that shower is not part of a π^0, the event is discarded.

With all of the cuts implemented, a clean sample is obtained with a reconstruction efficiency of 21%, and containing 12% background. After all of the cuts are set, the same reconstruction technique as the main analysis is performed. The result is the visible 4-momentum, comprised of the charged pion, with all unmatched showers subtracted, along with the tag from the beam.

4.6.2 Branching Ratio of $D^{\pm} \to K_L \pi^{\pm}$

Calculating the branching ratio utilizing this method provides a check on how well this method reconstructs the decay. The calculation is identical to that performed for the main analysis. The reconstruction efficiency, and amount of background that passes the cuts, will be calculated from MC. The Number of D's in the sample, and the number of events that pass all of the cuts will be measured from the data. The number of signal events is calculated by subtracting the appropriate amount of background, then dividing that number by the reconstruction efficiency. Dividing this number by the number of D's will give the Branching Ratio. Table 4.6 lists the numbers for this analysis. The BR is found to be 2.76%, this is compared to the PDG value of 2.82 $\pm$ 0.19. The numbers agree well, indicating that this analysis method is reasonable, and will give accurate information regarding the shower properties.

Table 4.6: BR($D^+ \to K_L \pi^+$)

MC	
# of K_L^0 in sample	2138
# of K_L^0 reconstructed	448
reconstruction efficiency	0.21
# of background counted as signal	55
% of reconstructed events that is background	0.12
Data	
total # of events	21853
# events reconstructed	144
# after background subtraction	126.32
# after divide by efficiency	602.82
Branching Ratio	2.76%
PDG	2.82% ± 0.19%

4.6.3 Properties of K_L^0 in Data

This study was run over datasets 31, 32, 33, and 35, for a total of 116 pb^{-1}. The first plot to be studied in data is the E_{Miss} vs. $Mass^2_{Miss}$ in Figure 4.28.

In agreement with the previous study of the interaction of K_L^0 in CLEO[27], approximately half of the K_L^0 do interact in the detector. Those that do not interact will not appear in the signal region, and can be easily eliminated.

The first property examined is the amount of energy deposited in the detector by a K_L^0. Figure 4.29 shows the amount of energy in the signal side showers, which

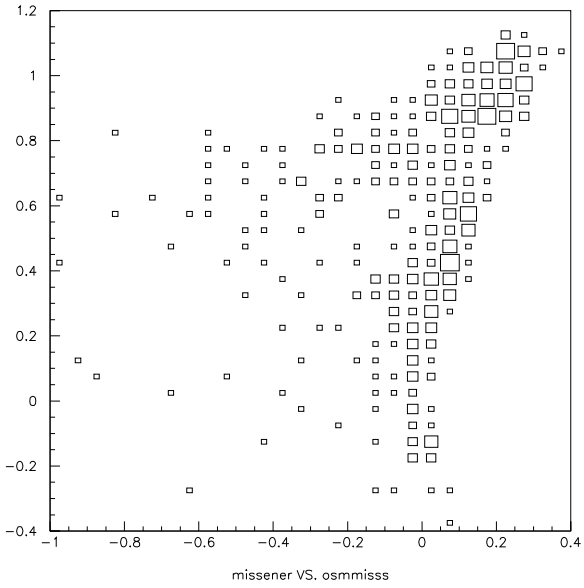

Figure 4.28: Data E_{Miss} vs. $Mass^2_{Miss}$

is equivalent to the amount of energy deposited by the K^0_L. Overall the spectrums are consistent, indicating that the MC is accurately simulating the amount of energy deposited in the detector.

Next an examination of the number of showers produced from the K^0_L is undertaken. Figure 4.30 plots the number of showers within cosθ of less than 0.8 around the missing momentum vector. With no other sources of missing momentum, the missing vector should point in the direction of the K^0_L. Approximately 55% of the events have a single shower in this region, while nearly 10% have two, and 30% have no showers.

Given the information gathered from the main analysis' examination of the plot of events with and without neutrinos (Figure 4.6) the best cut is $cos\theta < 0.55$. Figure 4.31 plots the closest shower angle for MC and for data. The value for K^0_L peaks at a value of one, with a tail extending out to 0.9. Given that the cut is far

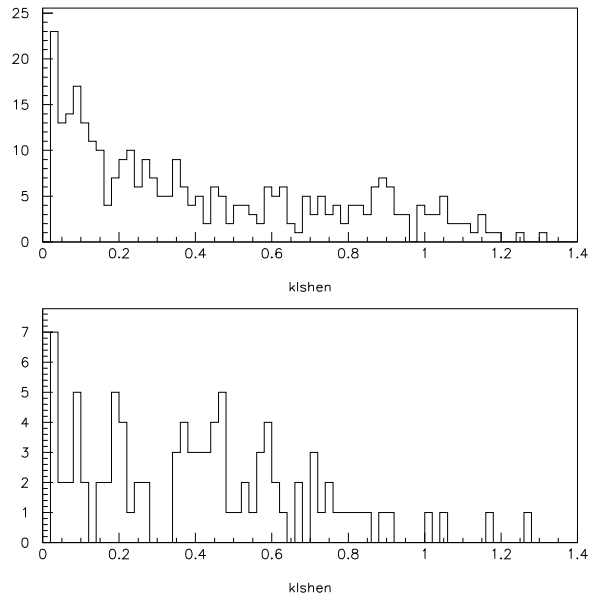

Figure 4.29: Energy of Showers from a K_L^0: Top - MC Bottom - Data

from the peak at one in K_L^0 events, any variance in the simulation between data and MC will not substantially affect the calculated branching ratio.

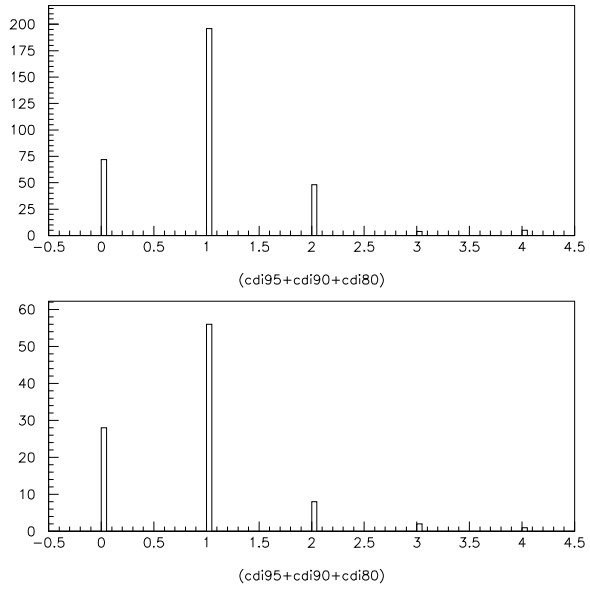

Figure 4.30: Number of showers with in costheta$>$ 0.8: Top - MC Bottom - Data

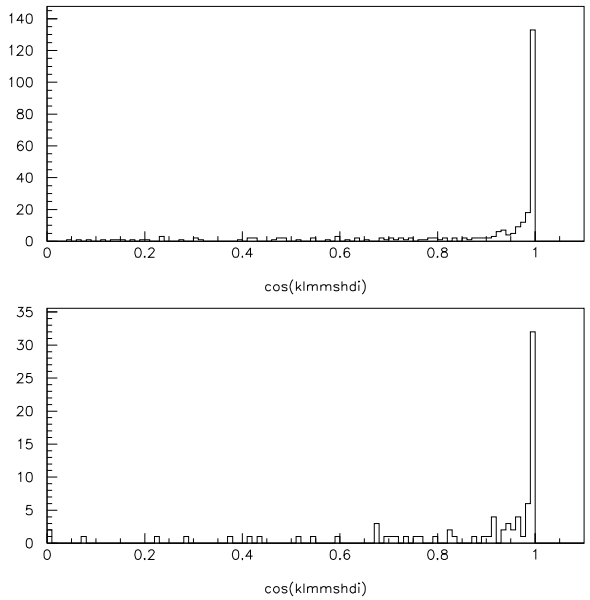

Figure 4.31: Closest Shower Angle from $D \to K_L\pi$ for Data and MC

Chapter 5

Results

5.1 Data - Monte Carlo Comparisons

Next is to make comparisons between MC and data for variables important to the analysis. This is important because the MC is used to determine the reconstruction efficiency for the analysis code, which is used in the calculation of the branching ratio. If there are errors in the MC simulation of the data, this will cause an error in the result.

5.1.1 Event Properties

Plots are made as a check on the quality of the MC as compared to the data. The plots of MC are scaled down by the ratio of the luminosity in data versus MC. The initial plots present the number of tracks and showers in an event (Figure 5.1), the costheta of the missing momentum vector (Figure 5.2), and the K_L^0 closest shower angle (Figure 5.3). These plots confirm that there is very good agreement between MC and data.

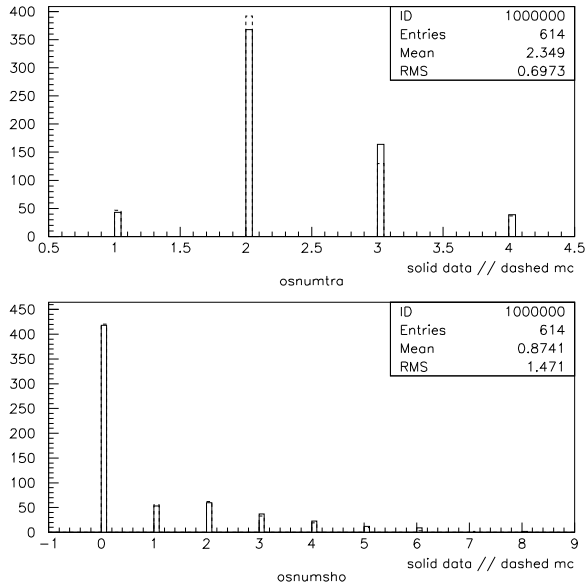

Figure 5.1: Number of Tracks in Event [top] Number of Showers in Event [bottom]: solid data - dashed MC (scaled)

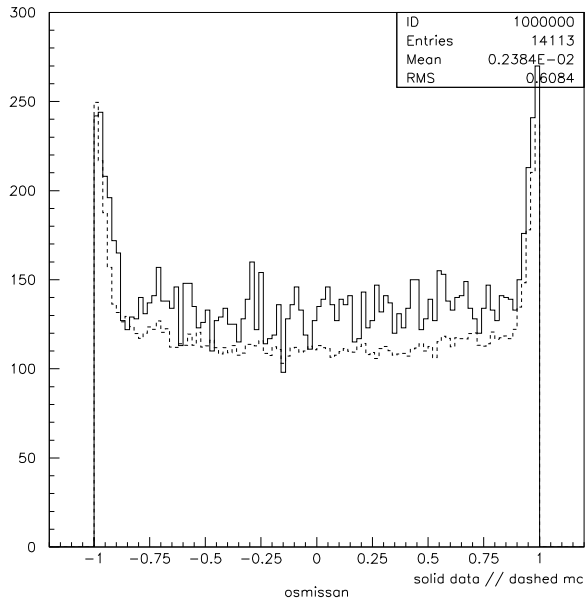

Figure 5.2: Costheta of Missing Momentum: solid data - dashed MC(scaled)

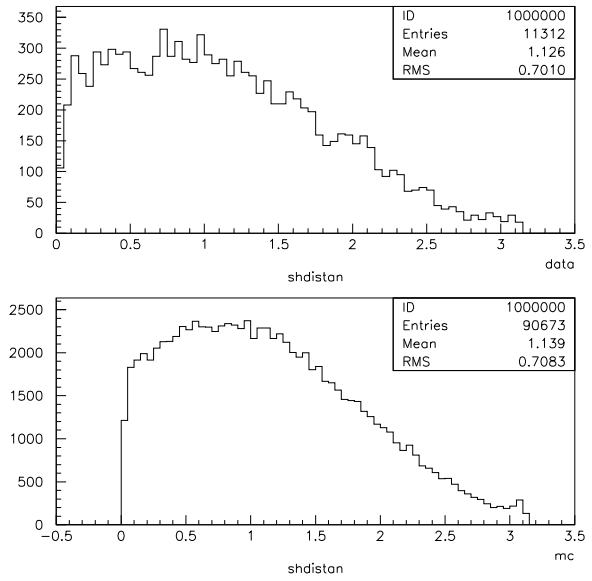

Figure 5.3: K_L^0 Shower Distance Angle: solid data - dashed MC(scaled)

5.1.2 Result Plots

The plots of E_{Miss} vs. $Mass^2_{Miss}$ (Figure 5.4) are very similar for data and MC. This provides confidence that the numbers obtained in MC can be used to get a reliable result for the branching ratio.

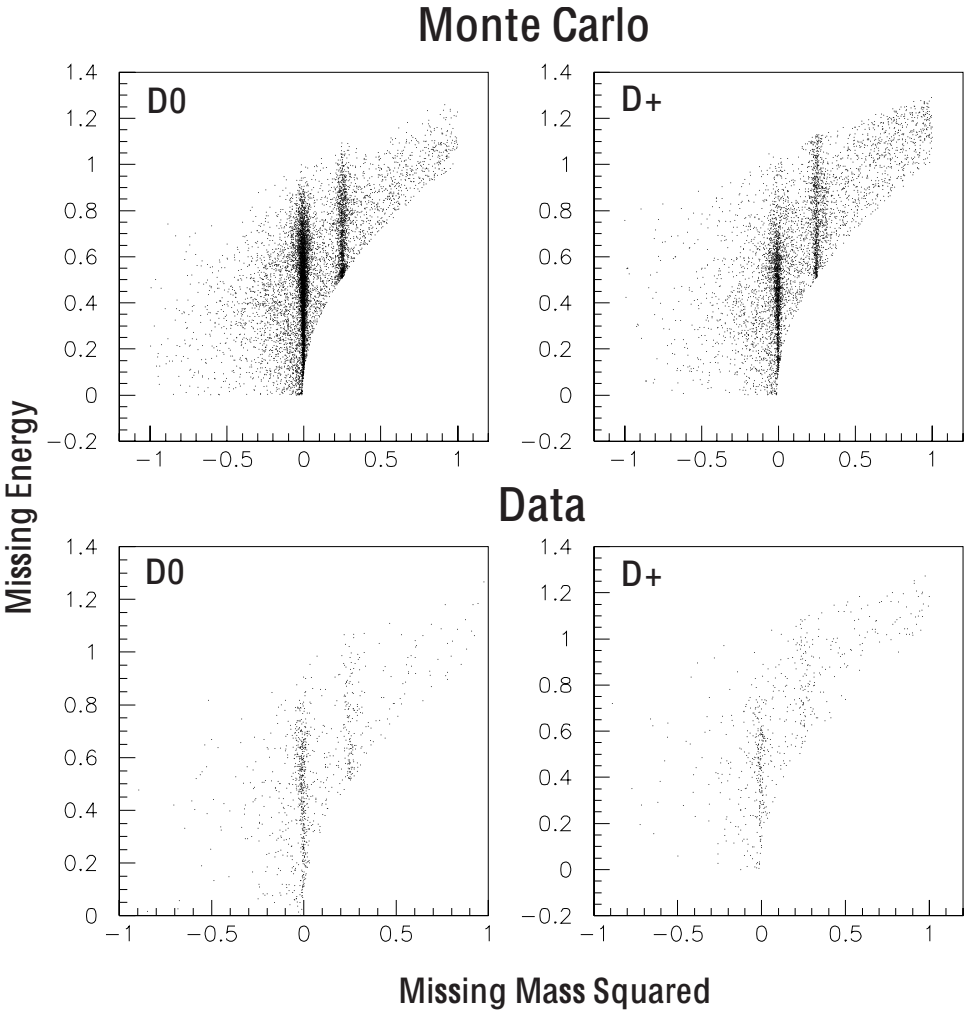

Figure 5.4: E_{Miss} vs. $Mass^2_{Miss}$ comparing Data vs. MC

The final plots examined are those of the missing energy spectrum, Figures 5.5 and 5.6. These are plotted separately for each dataset. On each plot, points are data, and the solid line represents MC scaled down by the ratio of luminocities. Figures 5.7 and 5.8 show a D_0 and D_+ plot for the combined datasets.

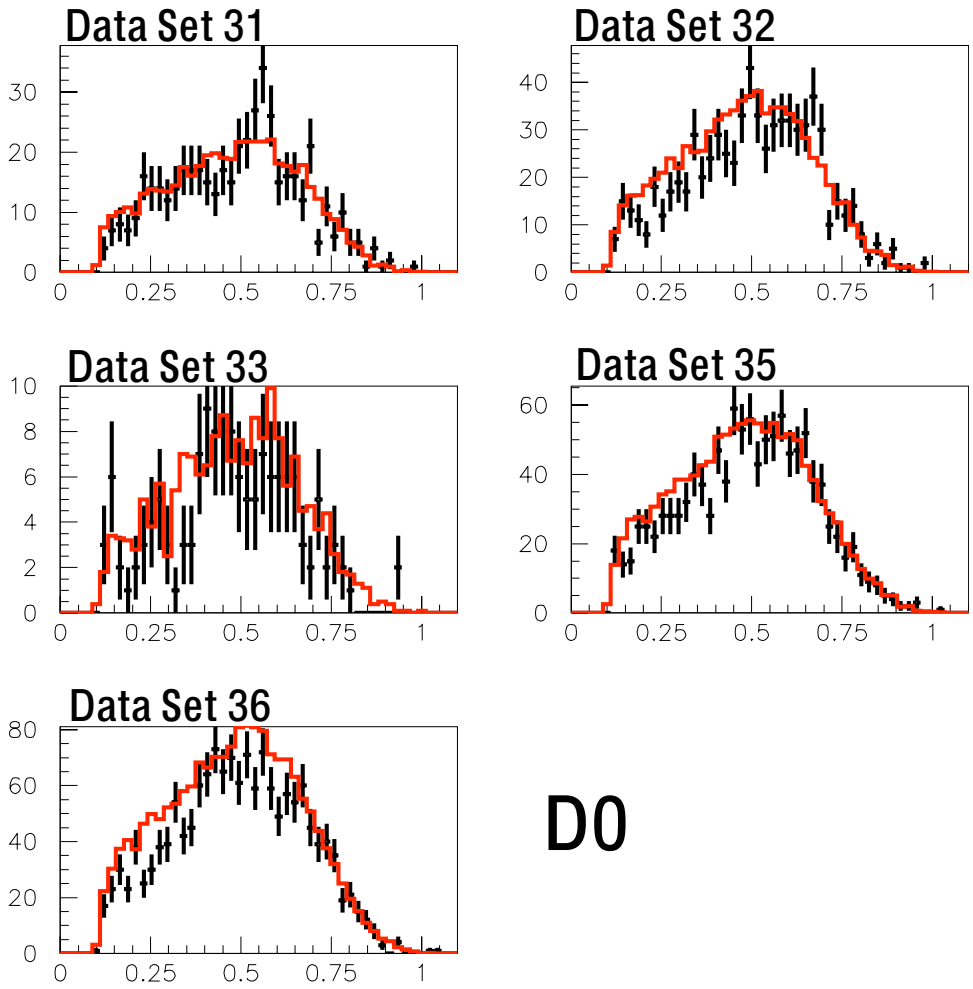

Figure 5.5: E_{Miss} spectrum by dataset: points data - solid MC(scaled)

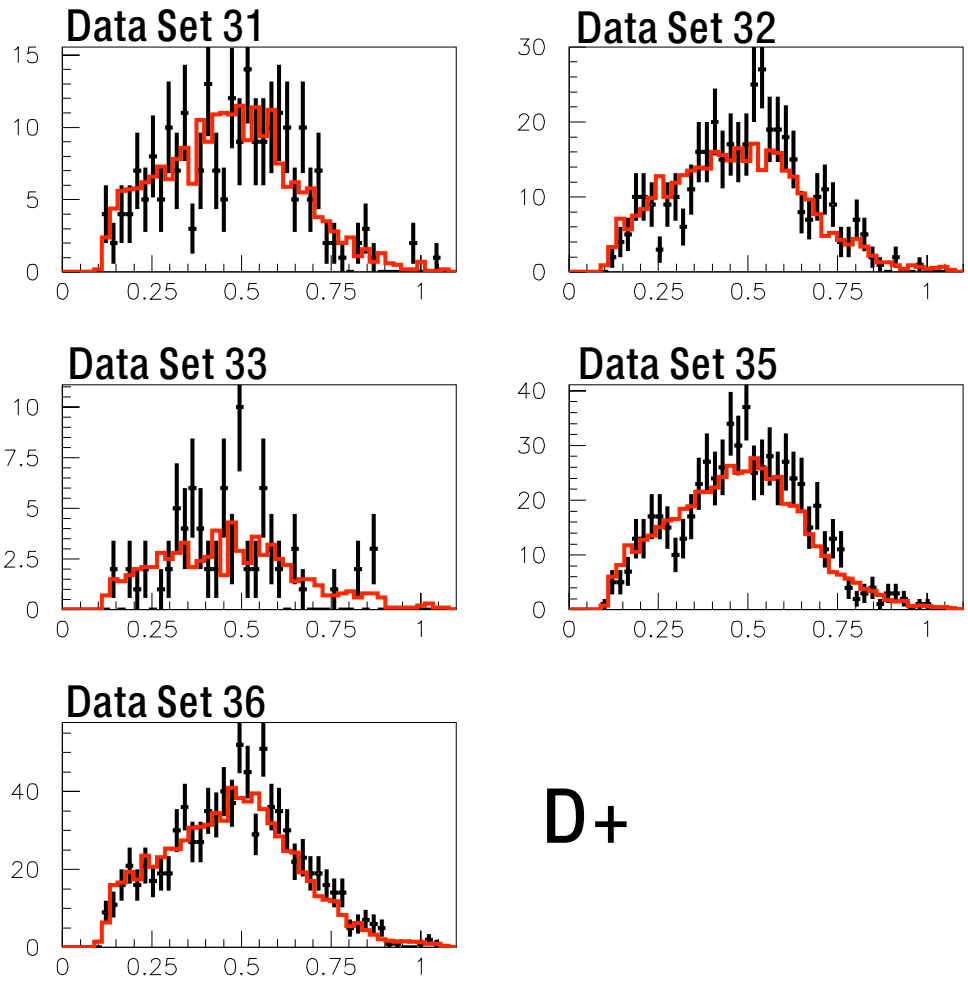

Figure 5.6: E_{Miss} spectrum by dataset: points data - solid MC(scaled)

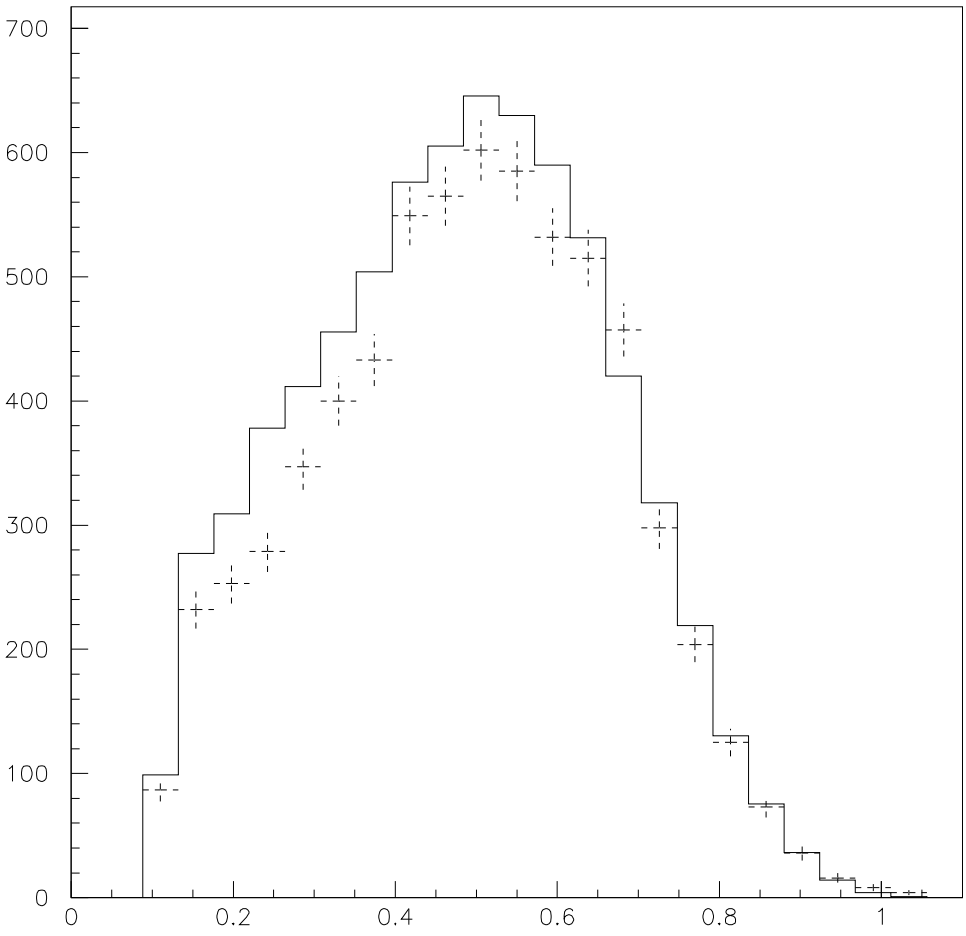

Figure 5.7: E_{Miss} spectrum for all datasets combined: points data - solid MC(scaled)

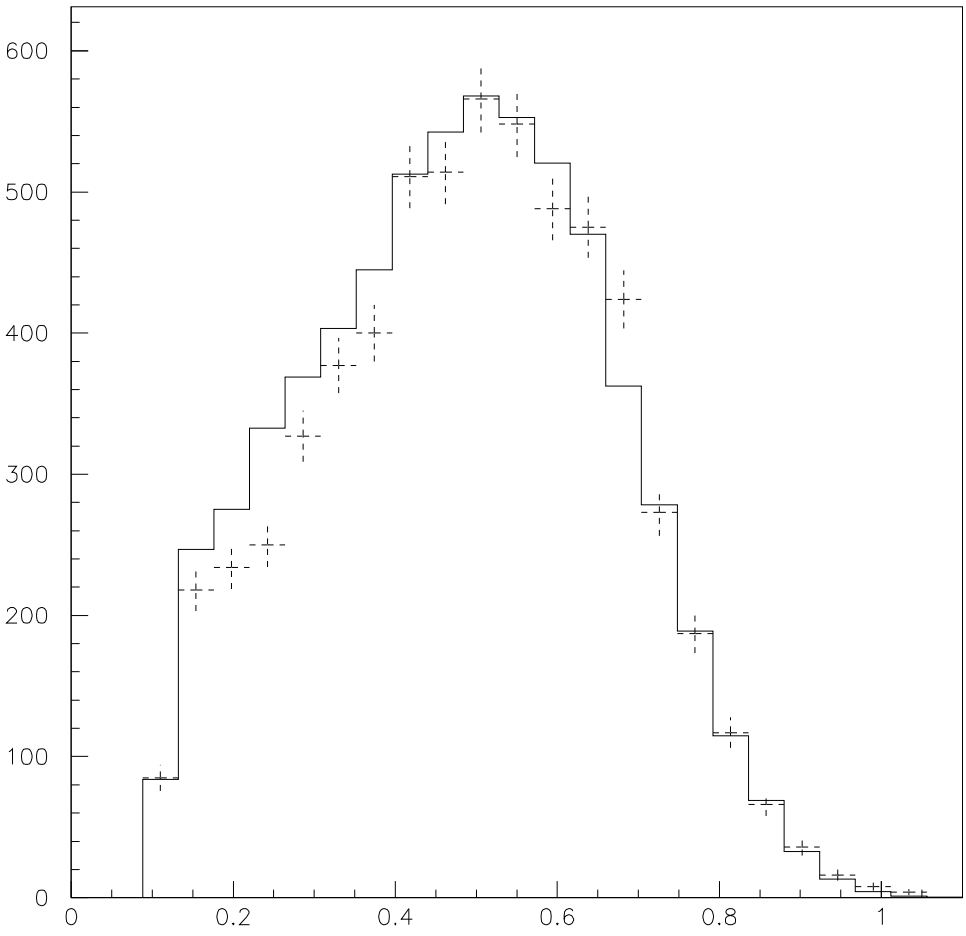

Figure 5.8: E_{Miss} spectrum for all datasets combined: points data - solid MC(scaled)

5.1.3 Mode Efficiency

A study of the efficiencies of the different semileptonic decay modes makes it clear that the spectrum produced by this analysis is not the true spectrum. There will be a different efficiency for each decay mode due to the different rates for different daughter particles. For example, the efficiency for $D \to Kl\nu$ is high, while $D \to K_L l\nu$ is very low. Tables 5.1 and 5.2 list the reconstruction efficiency for each decay mode that is used in the MC as a possible decay mode of a D.

Table 5.1: Efficiencies of Decay Modes D0; Including Their Conjugates

Mode	Efficiency %
D^0	28.8
$K^{*-}e^+\nu$	7.7
$K^-e^+\nu$	33.6
$K1^-e^+\nu$	5.0
$K2^{*-}e^+\nu$	2.8
$\pi^-e^+\nu$	36.3
$\rho^-e^+\nu$	15.1
$K^{*-}\mu^+\nu$	9.1
$K^-\mu^+\nu$	34.7
$K1^-\mu^+\nu$	4.4
$K2^{*-}\mu^+\nu$	3.1
$\pi^-\mu^+\nu$	38.7
$\rho^-\mu^+\nu$	18.7
Modes with K_L^0	7.8
Modes without K_L^0	33.3

Table 5.2: Efficiencies of Decay Modes D+; Including Their Conjugates

Mode	Efficiency %
D^+	12.0
$K^*be^+\nu$	13.1
$Kbe^+\nu$	10.1
$K1be^+\nu$	3.0
$K2^*be^+\nu$	3.9
$pi^0e^+\nu$	20.1
$\eta e^+\nu$	12.9
$\eta' e^+\nu$	8.0
$\rho^0 e^+\nu$	29.5
$\omega e^+\nu$	10.6
$K^*b\mu^+\nu$	14.1

Table 5.3: Table 5.2(Continued)

$Kb\mu^+\nu$	10.4
$K1b\mu^+\nu$	3.0
$K2^*b\mu^+\nu$	4.5
$\pi^0\mu^+\nu$	23.8
$\eta\mu^+\nu$	12.6
$\eta'\mu^+\nu$	11.9
$\rho^0\mu^+\nu$	31.4
$\omega\mu^+\nu$	10.0
$\mu^+\nu$	28.2
$\tau^+\nu$	5.8
Modes with K_L^0	11.2
Modes without K_L^0	18.5

5.2 Results

The final step in the analysis is to calculate a branching ratio for $D^{\pm} \to Xl\nu$ and $D^0 \to Xl\nu$. The branching ratios are listed in Tables 5.5 and 5.6. The detail on the method for calculating the numbers are discussd below.

5.2.1 Efficiency

The first number required to calculate a branching ratio is the efficiency for the cuts utilized in the analysis. This number is obtained by comparing the number of MC events with neutrinos with only one tag per event cut to the final number of neutrinos after all cuts. These numbers are found separately for $D^{\pm}$ and D^0, and for each dataset. For the total number of neutrino events, the cuts used are the one tag per event, a cut to have the D be charged or neutral, and a cut to require a ν in the event. For the number of ν with all cuts, all of the cuts described in the cuts section are used. The number of background events is found from the number of events that make it though all of the cuts, but have no MC truth table neutrino. The number of background events as a percent of the number of events that makes it through all of the cuts is then calculated. This percent is used to subtract off the number of background events in the sample in data after all cuts are applied.

The different data sets vary due to running and detector conditions. For these reasons the efficiency will vary with dataset. If the raw yield numbers were added together than the larger datasets would bias the final number. To reduce this effect the efficiency of the number of neutrinos and the amount of background are found for each dataset. Once the yield in data has been background subtracted

and corrected by the efficiency, the numbers are combined to get one number for the numerator for the branching ratio calculation. This process is also used for all of the calculations of the systematic errors - the datasets yields are combined, but only once the variation between each dataset is removed.

5.2.2 Number of D Particles In Sample

To accurately measure the branching ratio of the decay the number of D's that are in the large sample must be accurately measured. For the measurement being made here, the appropriate number is the number of D's in the tagged sample. As long as the number of D's is obtained from the tagged sample for both the MC and data, it is not necessary to measure the number of D's in the total sample.

The tagging efficiency appears in both the total number of D's, and the number of νs, and cancels out in the branching ratio. Given that this number is directly obtained from data there is no need to make a correction to it by dataset. The number of D's, after the background is subtracted out, is summed to make the denominator for the branching ratio.

$$BR = \frac{\text{Number of } \nu}{\text{total number of } D} \tag{5.1}$$

$$\text{Number of Observed } \nu = \text{Number of } \nu * \epsilon_{reconstruction} * \epsilon_{tagging} \tag{5.2}$$

$$\text{Number of tagged } D = \text{Total Number of } D * \epsilon_{tagging} \tag{5.3}$$

$$BR = \frac{\text{Number of Observed } \nu}{\text{Number of tagged } D * \epsilon_{r}econstruction} \tag{5.4}$$

There are five methods to count the number of D's, the variable used for cutting and fitting is the beam constrained mass of the D. The different methods will give

different values due to how they treat the background under the D signal peak. They will also cause different systematic errors. The five possible methods of counting the number of background events are:

- *Cuts* - The simplest way of counting the number of D's is to make all of the cuts, including one on the beam constrained mass. This does not subtract out any background.

- *Side Band Subtraction* - This method does not make a cut on the beam constrained mass. Instead, it counts the number of D's in the cut region, and then subtracts the number of events in a side band region of equal size.

- *Linear Fit to Background* - This counts the number of D's as in the side band subtraction method. The number of background events under the peak is calculated by making a linear fit to the events outside of the signal region, then extrapolating in and integrating over the signal region.

- *Argus Fit* - This is the same as the linear fit, but uses an Argus Function to model the background. The linear fit overestimates the amount of background at high mass due to the cutoff at the beam energy.

- *Fitting Peak* - This method fits the background and signal at the same time, and uses a Gaussian to fit the signal peak, and an Argus function for the background. This method introduces errors in the fitting of the signal, and systematics from the fit also.

  The tagged modes used for this analysis were selected to have the smallest amount of background. To illustrate the differences between the counting methods more clearly, Figure 5.9, shows the background fits for a cartoon version of the D mass plot.

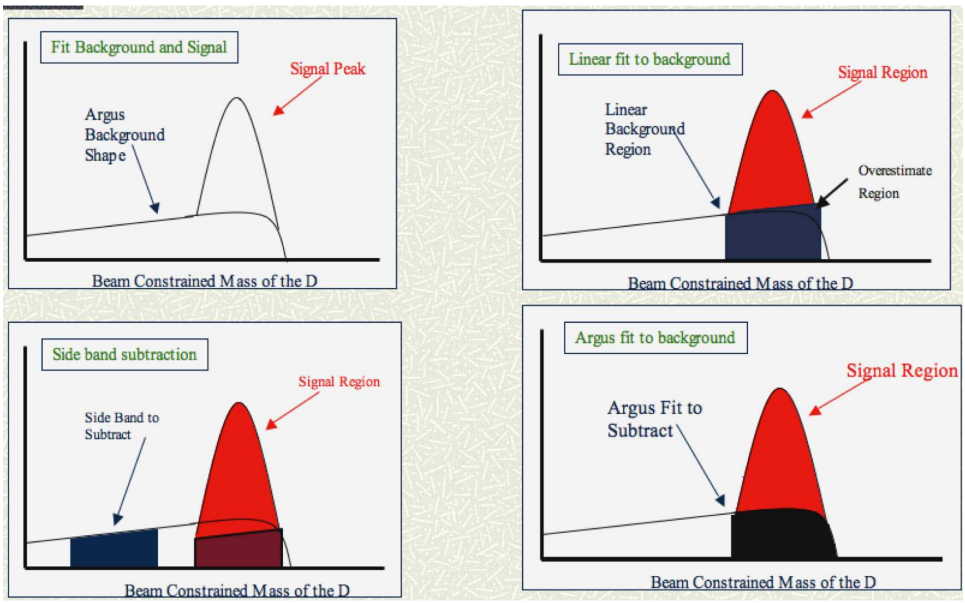

Figure 5.9: Cartoon drawings of the four methods of counting the background under the D peak

Table 5.4 shows the values obtained for the number of D's with each method. The *Cuts* method was not used, as it does not take into account the background in any manner and will over count the number of D's in the samples.

There is no significant difference in the number of D's obtained via the remaining four methods, and they give the expected results; those methods that eliminate more background also have a smaller number of D's. The background, as compared to the signal, is very small so the different methods do not vary significantly. The most accurate method, that introduces the least amount of extra error, is to count the number of events in the signal region, and then subtract the interpolated Argus function. Figure 5.10 shows the Argus fit to the background for data with the signal region having been suppressed in the plot. On this plot it is clea that the background decreases as the $Mass_{beamconstrained}$ approaches the limit of half of the E_{beam}. This decrease would be underestimated by the straight line fits or a side

Table 5.4: Numbers of D's with Different Counting Methods in Monte Carlo For Charged D's, for Datasets 31-33

	Side Band Subtraction	Argus	Linear	Fit
Number in Peak	139140	139140	139140	
Number Background	3919	4000	4500	
Number of D's	135221	135140	134640	134336

band subtraction.

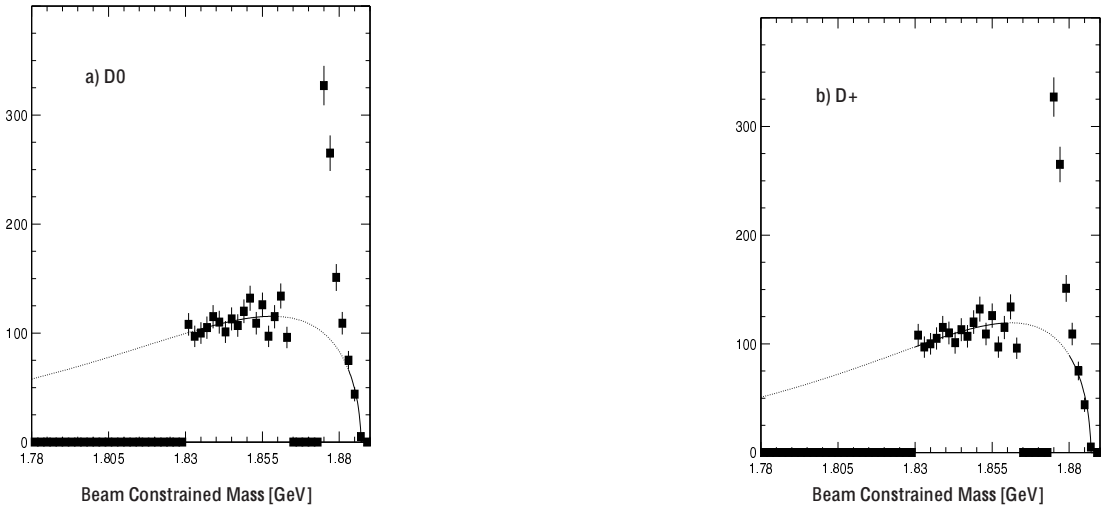

Figure 5.10: Argus Fits to Data Background in $Mass_{beamconstrained}$ for D^0 [Left] andD^+ [Right], with the signal peak suppressed

The background subtraction method is not used when counting the number of ν events. In Monte Carlo it is possible to review the particles that are produced in the generation of the event. Therefore, it is possible to tag the event when counting if the event has a neutrino or is a background event. This allows the counting to be done without worry about backgrounds. It also allows an accurate count of the

amount of background that remains after all of the cuts have been applied. The numbers obtained from the MC are the reconstruction efficiency which involves the number of neutrino events before and after the cuts are applied. Therefore, the number of D's is not needed for this measurement.

In data, the Argus background subtraction method is used to get a count of the D's in the sample. This number is combined with the amount of events after all cuts and the background is subtracted out to give the branching ratio. This is where an accurate count of the D's is needed, as any miscounting will directly affect the final result. The amount of background in the data signal sample is calculated from the MC sample, and scaled down by the ratio of luminosity.

5.2.3 BR

The last number needed to calculate the branching ratio is the number of reconstructed events in the data that pass all of the cuts. For each dataset the number of ν is subtracted by the number of background events, and then divided by the efficiency. This number is then divided by the total number of D's produced, and then combined into one number. As we are using the Dtag sample, only one half of each event has the possibility to decay freely. Therefore, the number of D events that are measured is the number of D's available to decay into a neutrino.

$$BR = \frac{(\#\nu - bkg)/(\epsilon_{recon})}{\#D's} \tag{5.5}$$

The final results, with statistical and systematic errors, and with the shift from the closest shower angle cut are as follows:

$BR(D^{\pm} \to X\nu) = 29.43\% \pm 0.83 \pm 1.75$

$BR(D^0 \to X\nu) = 13.52\% \pm 0.28 \pm 0.68$

5.2.4 Consistency Check Through f_D

Using HQE[11] the width for decay of a heavy meson to a final state is given as:

$$\Gamma(H_Q \to f) = \frac{G_F^2 m_Q^5}{192\pi^3}|KM|^2 \left[A_0 + \frac{A_2}{m_Q^2} + \frac{A_3}{m_Q^3} + \mathcal{O}(1/m_Q^4)\right] \tag{5.6}$$

When calculating a ratio of lifetimes the dominant order is $1/m_Q^3$ and not $1/m_Q^2$. There are no contributions of $\mathcal{O}(1/m_Q)$ due to exact cancelations between the initial and final states. These cancelations still act upon $\mathcal{O}(1/m_Q^2)$, giving them a smaller value than they would otherwise have. These cancelations do not arise once the calculations reach $\mathcal{O}(1/m_Q^3)$ so there is no reduction in strength for this term. It is therefore stronger than the suppressed $\mathcal{O}(1/m_Q^2)$.

The decay widths of D^0 and D^+ have the same contribution from the A_0 term, which is evident from the spectator diagram. The same is true of the A_2 term. The $1/m_Q^3$ however will introduce a difference in the lifetimes due to Pauli Interference, which is caused by two identical quarks being presentin the final state. The widths will then be

$$\Gamma(D^+) \simeq \Gamma_{spect}(D^0) + \Delta\Gamma(D^+) \tag{5.7}$$

$\Delta\Gamma(D^+) \simeq \Gamma_0 \cdot 24\pi^2(f_d^2/m_c^2)\kappa^{-4}\cdot$

$$\left[(c_+^2 - c_-^2)\kappa^{9/2} + \frac{1}{N_C}(c_+^2 - c_-^2) - \frac{1}{9}(\kappa^{9/2} - 1)(c_+^2 - c_-^2)\right] \tag{5.8}$$

With

$$\kappa = [\alpha_s(\mu_{had}^2)/\alpha_S(m_c^2)]^{1/b}, b = 11 - frac23N_f \tag{5.9}$$

It is then possible to get the ratio of the lifetimes, which can also be expressed in terms of the Semileptonic branching ratios.

$$\frac{BR(D^+ \to X\nu)}{BR(D^0 \to X\nu)} \simeq 1 + (\frac{f_D}{200MeV})^2 \tag{5.10}$$

Substituting the value of f_D found from the recent measurement of $D \to \mu\nu$, $f_D = 222.6 \pm 16.7^{2.8}_{3.4}$, yields a value for the ratio of branching ratios of 2.239 ± 0.856. The ratio of BR found from this analysis is 2.217 ± 0.169. These ratios agree very well, giving further confidence in the accuracy of the BR result.

Table 5.5: Efficiency and Branching Ratios for D^+

Data set	31	32	33	35	36	Total
MC						
# ν events	14905	24202	4663	73372	51947	
# ν after all cuts	1933	3064	597	9282	6678	
ν reconstruction eff.[%]	12.97	12.66	12.80	12.65	12.86	
# background events all cuts	374	554	122	1729	1294	
% of events that is bkg[%]	16	15	17	16	16	
Data						
# ν after all cuts	227	390	77	604	855	
background scaled by %	36.80	59.72	13.07	94.84	138.78	
(ν - scaled bkg) /eff	1466.60	2609.05	499.38	4024.78	5571.34	14171.13
# D's	5324	8752	1717	13346	19213	
# Bkg from Argus fit	109	193	32	324	402	
# D - Bkg	5215	8559	1685	13022	18811	47292
Branching Ratio with bkg sub	28.12	30.48	29.64	30.91	29.62	29.97

Table 5.6: Efficiency and Branching Ratios for D^0

Data Set	31	32	33	35	36	Total
MC						
# ν events	15832	25584	5185	80556	56422	
# ν after all cuts	4099	6778	1474	20928	14986	
ν reconstruction eff.[%]	25.89	26.49	28.43	25.98	26.56	
# background events all cuts	843	1272	276	4159	2978	
% of events that is bkg[%]	17	16	16	17	17	
Data						
# ν after all cuts	477	724	143	1141	1522	
background scaled by %	81.37	114.40	22.55	189.16	252.31	
(ν - scaled bkg) /eff	1528.10	2300.97	423.69	3663.83	4780.35	12696.94
# D's	10723	17402	3563	26584	38251	
# Bkg from Argus fit	1338	252	48	435	515	
# D - Bkg	9385	17150	3515	26149	37736	93935
Branching Ratio with bkg sub	16.28	13.42	12.05	14.01	12.67	13.52

Chapter 6

Systematic Errors

6.1 Systematic Errors

This analysis relies on the Monte Carlo accurately simulating the data in various critical ways. It is essential that accurate simulations are made of: the efficiency of reconstructing the events with neutrinos, and also the amount background that appears in the sample because it passed all of the cuts. If these numbers are different for MC and data, then the branching ratio will also vary. This section quantifies the error introduced by the systematic differences in data and MC. A number of systematic studies were conducted and their results are summarized in Table 6.1. This table also contains the total systematic error of 1.7 for $D^{\pm}$ and 0.7 for D^{0}.

Table 6.1: Summary of Systematics

Cause of Systematic	$D^{\pm}$ Error	D^0
Closest Shower Angle	0.246	0.053
0 charge	0.364	0.057
Single Track	0.205	0.010
Bad Shower	0.344	0.197
Bad ID	0.166	0.023
Splitoff Smearing	0.079	0.019
Vary V Nadir	0.493	0.065
Vary V Slope	0.208	0.137
Count BKG	0.043	0.015
Count Bcm Cut	0.171	0.120
Tag Eff	0.060	0.027
Track Finding	1.053	0.460
Track Smearing	1.060	0.388
MC Background	0.162	0.050
Total error	1.747	0.676

6.1.1 K_L^0: Closest Shower Cut

The closest shower cut relies on accurately modeling the shower production of a K_L^0 as it interacts, or does not interact, in the crystal calorimeter. If the shower production from K_L^0 is different in data and MC, then a shift in the branching ratio will occur as the cut is varied.

The closest shower cut is varied from -0.25 to 0.85 to determine the effect of the cut on the branching ratio. The result is a liner shift in the BR with respect to the cut. The equations for the liner fits are $y = -0.6904x + 30.116$ for D^+, and $y = -0.0893x + 13.604$ for D^0. With this shift, a correction will have to be made to the measured BR. Though not possible for this analysis, the simplest way to get the value of this shift would be to eliminate the cut and use the new BR value to shift the measured value by. Unfortunately this is not possible for this analysis, as the cos of the angle for K_L^0that peak very close to 1. Any errors in the simulation would appear If the cut was removed. To avoid this complication, the fit from -0.25 to 0.85 is extrapolated to 1, and this value is used to shift the BR.

Although the events containing a K_L^0 peak at one, other background is distributed throughout the plot. These non - K_L^0 events cause the systematic error shift in the BR when the cut is varied.

6.1.2 V cut

Most of the systematic errors result from the cuts affecting events in different regions of the E_{Miss} vs. $Mass^2_{Miss}$ plot differently in data and MC, and thus causing events to end up in a different region of the plot. As such the V cut, which

cuts directly on the plot, is a strong candidate to cause a systematic error. The cut can be varied in two ways: by vertically shifting the V up or down, or by varying the slope of the sides.

Nadir

The nadir of the V normally sits at zero in $Mass^2_{Miss}$ and at 100 MeV in E_{Miss}. Fully reconstructed events with no missing energy or missing mass will occur at the origin in the plot. However, due to mis-reconstruction, these events can smear and enter the signal region of the plot. A missing momentum cut of 100 MeVis useful in eliminating these events. As previously explained, a cut of 100 MeV will move the right hand cutoff line to the left, eliminating any events at zero $Mass^2_{Miss}$ with a missing energy of less than 100 MeV. Putting the nadir of the V cut at 100 MeVwill take the place of this missing momentum cut. The point of the V is decreased to 0 MeV and increased to 200 MeV to test the systematic error caused by this cut.

Slope of sides of V cut

Since the $Mass^2_{Miss}$ is equal to $E^2_{miss} - P^2_{miss}$, the error on the $Mass^2_{Miss}$ is proportional to $emiss$. A diagonal cut therefore acts on the constant fractional error. To vary the cut, $Mass^2_{Miss}$ is plotted for a slice of E_{Miss}. The value for the slice was chosen to be 500 MeV, as this is the middle value of the E_{Miss}. The window in E_{Miss} was 10 MeV wide. Both the sigma of the peak in $Mass^2_{Miss}$ as well as the number of sigma out the V cut is for this slice were measured. The slope of the line was then varied so that the value of the cut at 500 MeVwould shift by one sigma of the $Mass^2_{Miss}$ peak.

6.1.3 Error Study of Showers via Splitoff

This analysis is largely dependent on the accuracy of the modeling of showers in Monte Carlo. The reconstructed variables determine an event's location on the E_{Miss} vs. $Mass^2_{Miss}$ plot. If the showers are not modeled correctly then the shower could either be incorrectly passed by Splitoff, or incorrectly excluded. Either error could move the event into or out of the signal region. If the number of events in the signal region in the MC is not accurately reflective of the data, then the efficiency and number of background events subtracted off will be incorrect, causing a systematic error.

The Splitoff code uses a neural net to determine if a shower is a photon or splitoff. There is a function available to smear the output neural net before a decision is made to cut or keep a shower. The neural net values range from, photon-like at -1, to splitoff-like at +1. The smearing takes the form of:

$$NN \rightarrow NN' = s * |G| * |NN \pm 1|$$

NN is the neural net output, S is a scale factor of the smearing running from 0 to 1, G is a Gaussian distributed random number, with the + sign being applied to a photon-produced shower, and the - sign to all other showers. This smears photons to the splitoff-side, and splitoff showers to the photon-side. Since the smearing code looks up in the MC to determine if the shower is a photon or not for the smearing, this can only be done in MC. A value of 0.2[26] was used for this study, and the BR was recalculated.

6.1.4 Binary Cuts

Two binary cuts, which discriminate on a true/false variable, are used in this analysis. These cuts are: the requirement that the total charge of the event be equal to zero, and there not be a single track which is identified as a kaon. To find the error, one by one each cut is removed, and the shift in BR is measured. The results are summarized in Table 6.1.

6.1.5 Shower Angle Cut

This cut eliminates events which have a shower with a $cos\theta$ greater than 0.8, when the shower is not part of a π^0. This cut is used to eliminate the extraneous showers that Splitoff introduces when it cannot perform the required sums of crystals when the shower is on the detector's border. To see how this cut varies with good showers, the BR is calculated for the cut at four values between 0.6 and 0.8. The values, excluding 0.8, are linearly fitted and then extrapolated to 0.8. This difference between the extrapolation and the fitted value is the error.

6.1.6 D Counting

Differences in the number of D's that are used to get the branching ratio can also cause a shift. The calculation of the number of D's has two components: the number of events in the peak, and the number of events subtracted.

The number of events in the peak is found by counting the events in a wide window of B_{CM}. The values used for this counting are 1.860 to 1.869 for D^0 and 1.866 to 1.873 $D^{\pm}$. The distribution has a sigma of 1.8 MeVforD^0, and 1.4 MeVfor

$D^{\pm}$, which is used to vary the cuts, both in the plus and minus direction.

The other variable that can be varied is the amount of background subtracted from the number of events in the signal region. An Argus shape is used to interpolate the amount of background under the signal peak. The amount of background is varied up and down by the statistical error on the number of background.

6.1.7 Efficiency Cancelation

When the BR is calculated, it is assumed that the overall tagging efficiency is the same as the tagging efficiency for semileptonic decays. This allows the tagging efficiency to be canceled out. However, when the semileptonic decays are selected it affects the overall event topology and can have an effect on the tagging efficiency if it is not simulated correctly in MC. A study was performed[30] on how the difference in multiplicity between data and MC affect the tagging efficiency. It was found to cause a 0.2% error. This error was put into the calculation of the branching ratio, and the resulting shift was calculated.

6.1.8 Reconstruction Errors

Another way in which events could be improperly shifted into or out of the signal region is due to the mis-identification of the type of charged particles in the event. The track is tested to see if it is an electron. If not it is tested to see if it is a kaon, and if it fails both of these identifications, then the track is defaulted to a pion for the momentum sums. To test how much of an effect the mis-identification has on the value, the amount of badly identified particles for each type, is doubled.

The amount of each type of particle that is mis-identified is obtained from the Monte Carlo. The particle is tagged in the MC and the type of identification that the analysis code assigns it is recorded. In this manner the percent of bad identifications can be found. For kaons, 1.56% are not identified and are defaulted to pions. The percent of not identified electrons, which are then treated as pions, is 23.92%. Since there is no identification for pions, the mis-identification now occurs when the code to identification kaons mistakenly assigns them as kaons.

To get the error from reconstruction, the amount of badly identified particles for each type is doubled. These particles to be mis-identified are picked via a random number generator.

6.1.9 Errors from MC Simulation of D Decays

Another possible error comes from the simulation of the decays of the D in the MC. Each decay mode has, due to the differing decay products, a different reconstruction efficiency. If the MC branching ratios are not correct then the total reconstruction efficiency will be also incorrect. To obtain the error for these possible shifts, each decay mode is shifted by the average error for the measured branching ratios for the flavor of D it comes from. This shift is 5% for D^0 and 10% for D^+. The shift in the inclusive BR is found for each decay mode, and summed in quadrature to obtain the full error.

Another possible source of error is how MC assigns the energy of the D to the daughter particles. This error has the greatest effect on $d\Gamma/dQ^2$, which is the dependence of the decay rate as a function of the energy given to the W. To study this effect, the energy spectrum was compared for data and MC. To achieve a

clean comparison, the spectrum for electrons was used. By using data events that contain only one track which is identified as an electron, a pure sample can be obtained in data to compare to MC. No difference is seen in the spectra, so there is no systematic error from this part of the reconstruction.

6.1.10 Tracking

The handling of tracks creates two errors that must be accounted addressed, The first deals with the track finding efficiency. To measure the difference between MC and data, a study was performed of the decay $\psi' \rightarrow J/\psi$, with the J/ψ decaying to a charged lepton pair. The mass difference between the dilepton system and the mass of the J/ψ must be less than 50 MeV. Once the dilepton pair is combined into a J/ψ, it is combined with a pion to make a ψ' candidate. Another good pion is then searched for to make a full reconstruction. The mass difference of the candidate compared to the J/ψ has to be within 50MeV of the mass difference of the two ψ states to be considered to have found a track.

The missing mass of the ψ candidate, which will be the difference between it and the ψ', is then fit for the cases where the track was and was not found. The efficiency is found by $Eff = \frac{N_{seen}}{N_{seen}+N_{missed}}$. This efficiency is found for data and MC, with the difference being 1%. To get the systematic error, the MC files are analyzed, with 1% of randomly selected tracks being dropped. The new BR is calculated and used to obtain the systematic error.

The second error from tracking is the amount of smearing to the track momentum due to the resolution simulation in MC. The momentum of each track is

additionally smeared by:

$$p' = p + s\delta p, with \delta p = p_{recon} - p_{true} \tag{6.1}$$

The smearing for this study was taken to be 10%, which was the value used by CLEO III. As the tracking is at worst the same in CLEO-c, and in most cases better, this is a conservative estimate.

Chapter 7

Conclusion

Using the extremely clean data taken at CLEO-c, this analysis measured a D semileptonic decay by a new method. For the first time is it is possible to identify events through their properties indicating that they contain a neutrino. Since this measurement is independent of other semileptonic measurements, it can be used as a cross check, on other inclusive measurements, and on the sum of exclusive modes. Semileptonic decays are important as they allow extractions of theoretical variables, such as CKM matrix elements like V_{cd} and decay constants like f_D. This method allows for an orthogonal measurement of the total branching fraction which can be used to make sure that the overall sum of measurements is consistent.

One of the questions before this analysis was performed was how well it would be possible to separate out the signal from background using only the cuts on the missing variables. Previous semileptonic decays utilizing the method of neutrino reconstruction would retune the missing momentum. The missing momentum vector would be tuned to get the best variables for the event before it was utilized to reconstruct the signal side. Due to the cleanliness of the events at the $\psi(3770)$, and the knowledge about the detector gained through years of running in the B regime, it is possible to measure and select events from the non-tuned missing momentum vector.

Another concern was background from K_L^0 , which can also cause events to have missing energy and momentum. Since CLEO-c has no hadronic calorimeter,

it was not known if the K_L^0 background would be too high to successffully make a measurement. Fortunately, The non-interacting K_L^0 can be eliminated through the V cut. Using the closest shower angle cut most of the K_L^0 that do interact can also be eliminated. With a combination of these two cuts the number of K_L^0 containing events can be reduced to a manageable level.

By obtaining a good measurement of the Branching Ratio using the neutrino reconstruction method, this analysis also proves how well this method works. This analysis only uses the neutrino reconstruction to find its events, and has no backup method to help select the events. The fact that this method works so well indicates a very good knowledge of the detector, and lends strength to the validity of other measurements that use this method. With more statistics, it will be possible to measure the semileptonic neutrino energy spectrum. This will allow a check to be made against theoretical calculations, which until now could only be tested against the charged lepton spectra.

In the the future, with more luminosity, this measurement can be even more precise. This will allow an extraction of the moments of the spectrum which can then be used to extract basic physics constants.

REFERENCES

[1] M.K. Gaillard, B. Lee, *Phys. Rev.* **D 10** (1974) 897.

[2] B. Richter, in: Proceed. of the XVII Intern. Conf. on High Energy Physics, London, July 1974, J.R. Smith (ed.), Rutherford Lab., Chilton, England, 1974, pp. IV-37-55.

[3] J. J. Aubert et al., *Phys.Rev.Lett.* **33** (1974) 1404.

[4] J. E. Augustin et al., *Phys.Rev.Lett.***33** (1974) 1406.

I.I. Bigi, M. Shifman, N.G. Uraltsev, *Annu. Rev. Nucl. Part. Sci* **47** (1997) 591.

[5] G. P. Lepage and P. B. Mackenzie, *Phys. Rev.* **D 48**, 2250 (1993).

[6] See for example: M. Alford et al., *Phys. Lett.* **B 361**, 87 (1995); M. Luscher et al, Nucl. *Phys.* **B 478**, 365 (1996).

[7] N. Isgur, D. Scora, B. Grinstein, and M.B. Wiss, *Phys. Rev.* **D 39**, 79 (1989).

[8] K. Wilson, *Phys.Rev.* **179** (1969) 1499.

[9] I.I. Bigi, M. Shifman, N.G. Uraltsev, *Annu. Rev. Nucl. Part. Sci* **47** (1997) 591.

[10] B. Guberina, S. Nussinov, R. Peccei, R. Rückl, *Phys.Lett.* **B 89** (1979) 261.

[11] Bianco, Fabbri, Benson and Bigi, *A Cicerone for the Physics of Charm*, hep-ex/0309021.

[12] I.I. Bigi, N.G. Uraltsev, *In. J. Mod. Phys.* **A16** (2001) 5201.

[13] I.I. Bigi, N.G. Uraltsev, *Z. Phys.* **C 62** (1994) 33.

[14] I.I. Bigi, N.G. Uraltsev, *Phys.Lett.* **B 280** (1992) 271.

[15] M. Artsuro *et al. Improved Measurement of* $B(D^+ \to \mu^+\nu)$ *and the Pseudoscalar Decay Constant* f_{D^+}, hep-ex/0508047.

[16] D.J. Lange, Nucl. Instrum. Methods Phys. Res., Sect.**462**, 152 (2001).

[17] R. Brun *et al.*, Geant 3.21, CERN Program Library Long Writeup W5013 (1993), unpublished.

[18] CLEO III (general): G. Viehhauser *CLEO III Operation*, Nucl. Instrum. Methods A **462**, 146 (2001).

[19] CLEO III RICH: M. Artuso *et al.*, *Construction, Pattern Recognition, and Performance of the CLEO III LiF-TEA RICH Detector*, Nucl. Instrum. Methods Phys. Res., Sect. A **502**, 91 (2003); hep-ex/0209009. Also see: M. Artuso *et al.*, *The CLEO RICH Detector*, physics/0506132.

[20] CESR-c, ZD: R.A. Briere *et al.* (CESR-c and CLEO-c Taskforces, CLEO-c Collaboration), Cornell University, LEPP Report No. CLNS 01/1742, 2001 (unpublished).

[21] CLEO III DR3: D. Peterson *et al.*, Nucl. Instrum. Methods Phys. Res., Sect. A **478**, 142 (2002).

[22] CLEO III trigger: M.A.Selen, R.M.Hans and M.J. Haney, IEEE Trans. Nucl. Sci. **48**, 562 (2001). "The CLEO-III Trigger: Level 1 Decision and Gating" R.M.Hans, C.L. Plager, M.A. Selen and M.J. Haney, IEEE Trans. Nucl. Sci. **48**, 552 (2001).

[23] R. Brun *et al.*, "GEANT 3.15: Detector description and simulation tool," CERN Report No. DD/EE/84-1 (1987) (unpublished).

[24] CBX 01-47.

[25] CBX 96-103 and www.lns.cornell.edu/ñea9/trkman.htm.

[26] www.lns.cornell.edu/c̃leo3/development/src/SplitoffProd/Doc.

[27] CBX 97-70.

[28] Sun, Werner, D Hadronic Branching Fraction Fits, talk at July CLEO Meeting.

[29] CleoAC CLEOc sample web page.

[30] CBX 05-08.